THE PENNSYLVANIA STATE UNIVERSITY
SCHREYER HONORS COLLEGE

DEPARTMENTS OF PHYSICS AND ASTRONOMY & ASTROPHYSICS

Unassociated Candidate TeV Sources from The HAWC Observatory

NICOLE MICHELLE FIRESTONE
SPRING 2021

A thesis
submitted in partial fulfillment
of the requirements
for baccalaureate degrees
in Physics and Astronomy & Astrophysics
with interdisciplinary honors in Physics and Astronomy & Astrophysics

Reviewed and approved* by the following:

Miguel A. Mostafá
Professor of Physics and Astronomy & Astrophysics
Thesis Supervisor

Richard W. Robinett
Professor of Physics
Associate Department Head
Honors Adviser

William N. Brandt
Verne M. Willaman Professor of Astronomy & Astrophysics
Honors Adviser

*Electronic approvals are on file.

Abstract

As neutrally-charged astrophysical messengers, gamma rays serve as powerful tools for determining the origins of incredibly high-energy particles from across our universe [1]. Gamma rays are considered to have the highest energy of all electromagnetic radiation, with energies spanning from 0.5 MeV to about 100 TeV [2]. Although lower-energy gamma rays can originate from within our solar system, gamma rays in the GeV and TeV ranges tend to originate from sources beyond our solar system [1]. By investigating these sources, we can understand more about the astrophysical phenomena that characterize the most extreme conditions in our universe, such as supernova remnants, gamma-ray bursts, and pulsars [3]. The High Altitude Water Cherenkov Gamma-Ray Observatory (HAWC) is one of the most sensitive gamma-ray detectors in the very high energy (VHE) regime, with the capability to observe gamma rays from 100 GeV and 100 TeV [4]. In 2017, HAWC conducted a blind search encompassing two thirds of the sky and 508 days of observations [4]. In this search, there were 16 VHE gamma-ray excesses that were unassociated with any previously discovered gamma-ray sources [4]. Now with data from 1523 days of observations, we begin to study these 16 unassociated candidate TeV sources in more detail. In this work, we update the locations of maximum significance for these candidate TeV sources and analyze the temporal progression of their significance and flux. This allows us to determine if they have faded into the diffuse gamma radiation or if they can still be considered unassociated candidate TeV sources. We then reevaluate the morphologies and spectral energy distributions of the remaining sources and discuss any recent observations from other gamma-ray observatories. We find that 10 of these 16 unassociated candidate TeV sources can still be considered candidate sources. In the future, we plan to use data from other observatories to continue to put better constrains on the morphology and spectral energy distributions for these sources and better understand their acceleration mechanisms. In addition, we plan to conduct a similar investigation with new HAWC excesses discovered with recent data from 1523 days of observations [5]. By investigating these excesses in the high-energy gamma-ray sky, we can discover and characterize new extreme astrophysical phenomena and ultimately uncover valuable information about the physical mechanisms that accelerate particles to very high energies.

Table of Contents

List of Figures

List of Tables

Acknowledgements

First and foremost, I would like to thank the Penn State Departments of Physics and Astronomy & Astrophysics and the Schreyer Honors College for providing me with the means to reach my full potential as an undergraduate student, and the Office of Science Engagement in the Eberly College of Science at Penn State for awarding me with a grant to pursue my research in the Spring of 2020. I would like to thank Dr. Richard Robinett for being a constant source of encouragement and kindness to me throughout my undergraduate career. I would like to thank Dr. Miguel Mostafá for being an incredible mentor and always pushing me to challenge myself as a researcher and science communicator. I would like to thank my research partner and friend, Sarah Greberman, and the rest of the HAWC team for helping me grow as a scientist and giving me a home at Penn State. I would like to thank Dr. William Brandt for being a resource and support to me throughout this process. And lastly, I would like to thank my family and close friends for always reminding me that I can accomplish anything when I put my mind to it. I would not be where I am today without the support and care of these individuals, and I will forever be grateful for their presence in my life.

CHAPTER 1

Introduction

1.1 High-Energy Gamma-Ray Astronomy

Gamma rays reside in the most energetic portion of the electromagnetic spectrum. For this reason, we can use gamma rays to probe astrophysical phenomena that characterize the most extreme conditions of our universe where particles are accelerated to incredibly high energies. Since gamma rays are a type of electromagnetic radiation, we correlate their energy, wavelength, and frequency by Plank's relation. In Equation 1.1 we present Plank's relation where E is the energy of the radiation, h is Plank's constant equivalent to 4.136E-15 eV·s, ν is the frequency of the radiation, c is the speed of light in a vacuum equivalent to 3×10^{10} cm/s, and λ is the wavelength of the radiation. Gamma rays correspond to electromagnetic radiation in the energy range above $\sim$ 0.5 MeV.

$$E = h\nu = \frac{hc}{\lambda}, \tag{1.1}$$

Since gamma rays are a type of electromagnetic radiation, they do not hold charge. For this reason, they cannot be accelerated by electric fields or magnetic fields. However, there are many acceleration mechanisms in extreme astrophysical objects that result in the emission of gamma rays. Gamma-ray emission processes fall into two categories: leptonic emission and hadronic emission. Leptonic emission occurs when accelerated electrons/positrons produce gamma rays, while hadronic emission occurs when accelerated protons produce gamma rays. Together, the gamma rays produced through these processes make up the unique spectral energy distributions of astrophysical sources such as supernova remnants, gamma-ray bursts, and pulsars. Gamma ray spectral energy distributions serve as valuable clues for determining the acceleration mechanisms and classifications of extreme astrophysical phenomena.

1.1.1 Leptonic Emission

There are two primary gamma ray production mechanisms that fall into the class of leptonic emission: leptonic synchrotron radiation and inverse Compton scattering.

Leptonic Synchrotron Radiation

Leptonic synchrotron radiation is produced when extremely relativistic electrons are accelerated by a magnetic field. In Equation 1.2, we model the simple case in which a population of

electrons with energy E_e radiates photons with an isotropic distribution of pitch angles [6]. In this case, the energy of photons produced via leptonic synchrotron emission is characterized as E_{synch}, where B is the strength of the magnetic field and E_e is the energy of the electron.

$$E_{synch} = 0.2\frac{B}{10\mu\text{G}}\left(\frac{E_e}{1\text{TeV}}\right)^2 \text{eV} \tag{1.2}$$

Contrary to our assumption, a population of electrons does not tend to have uniform energy distribution. The initial distribution of electron energy can be better approximated by a power law of index α_e [6]. In Equation 1.3 we present a simple representation of a power law, where y is the dependant variable, k is a constant, x is the independent variable, and α is the power law index.

$$y = kx^{\alpha} \tag{1.3}$$

With this approximation for the distribution of electron energy, we can accurately characterize the initial spectral energy distribution due to synchrotron emission with a simple power law of index $\alpha_{synch} = \frac{\alpha_e+1}{3}$ [6]. As electrons produce photons via synchrotron radiation, they lose energy and cool [7]. When the cooling timescale of the electrons becomes comparable to the age of the source, we experience a correlated break in the synchrotron power law spectrum (see Figure 1.1) [6]. Here, α_{synch} becomes $\frac{\alpha_{e'}+1}{3}$, where $\alpha_{e'}$ is the power law index of the cooled electrons. Studying the synchrotron spectrum of an astrophysical source can help us to better understand the strength and effects of its magnetic field.

Inverse Compton Scattering

In addition to leptonic synchrotron radiation, gamma rays can also be emitted through inverse Compton scattering. Inverse Compton scattering is a process in which a relativistic electron e^- scatters a lower energy photon λ to very a high energy photon within the x-ray or gamma-ray regime λ' [8].

$$e^- + \lambda \rightarrow \lambda' \tag{1.4}$$

When a lower energy photon is up-scattered by an electron, it's wavelength changes according to Equation 1.5, where λ_C is known as the Compton wavelength equivalent to $\frac{h}{m_e c}$ and θ is the scattering angle of the photon.

$$\Delta\lambda = \lambda_C(1 - \cos\theta) \tag{1.5}$$

In Equation 1.6 we present the energy produced by Inverse Compton Scattering E_{IC}, where E_λ is the energy of the incident photon and E_e is the energy of the electron.

$$E_{IC} = 5 \times 10^9 \frac{E_\lambda}{10^3\text{eV}}\left(\frac{E_e}{1\text{TeV}}\right)^2 \text{eV} \tag{1.6}$$

In the case of inverse Compton scattering, the power law approximation for the distribution of electron energy yields a power law index of $\alpha_{IC} = \frac{\alpha_e+1}{2}$ in the Thompson regime and a power law index of $\alpha_{IC} = \alpha_e + 1$ in the Klein–Nishina regime (see Figure 1.1) [6].

When the photons emitted via synchrotron radiation are up-scattered via inverse Compton scattering, the spectral energy distribution of a source will reflect a process called synchrotron self

Compton. In the case of synchrotron self Compton, the spectral energy distribution of the synchrotron radiation will be mimicked at higher energy in the spectral energy distribution of inverse Compton scattering [7]. That being said, there are many external types of photon fields that undergo inverse Compton scattering aside from synchrotron radiated photons. Studying the inverse Compton spectrum can help us to better understand the nature of these external photon fields, which we can use to better characterize astrophysical sources.

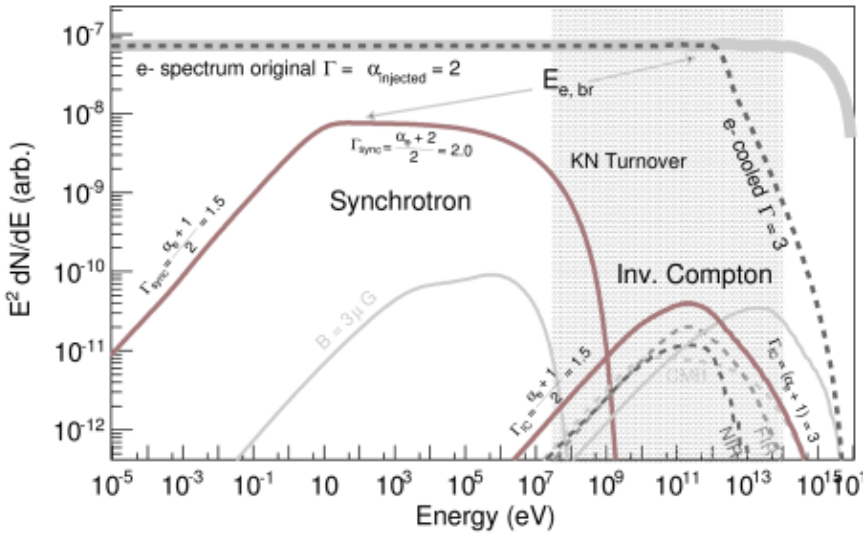

Figure 1.1: Leptonic Gamma-Ray Emission [6]

1.1.2 Hadronic Emission

Pion Decay

The primary source of hadronic gamma-ray emission is known as pion decay. Pion decay is a process in which neutral pions π^0 decay into two gamma rays γ.

$$\pi^0 \rightarrow \gamma + \gamma \tag{1.7}$$

When pions decay from rest, the gamma rays produced have a combined energy equivalent to the rest mass energy of a pion $m_\pi c^2$ (see Equation 1.8), where m_π is the rest mass of a pion.

$$E = mc^2 \tag{1.8}$$

Gamma rays resulting from pion decay produce a log-log spectrum with a peak at 67.5 MeV [8]. This spectral feature is commonly referred to as the "pion-decay bump" (see Figure 1.2). In astrophysical source, pion decay is often related interactions between hadrons and ambient gas [9]. Since ambient gas is only present in certain astrophysical sources (such as mid-aged supernova remnants), the presence of pion decay can be a valuable tool for source classification [9, 10].

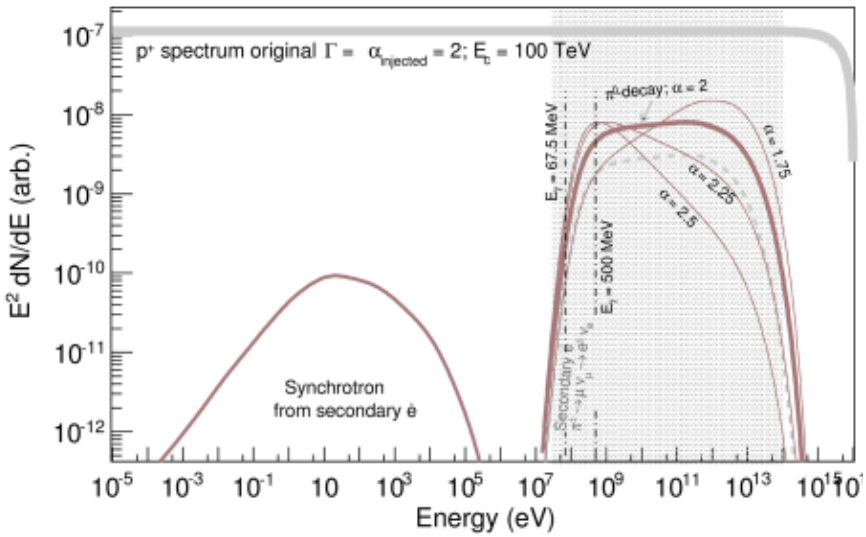

Figure 1.2: Hadronic Gamma-Ray Emission [6]

1.2 Gamma-Ray Detection Techniques

Since gamma rays are a type of light particle, or photon, they do not carry a charge. For this reason, gamma rays are able to travel through space in straight paths from their origins, uninhibited by magnetic fields. This allows us to reconstruct the arrival directions and energies of gamma rays and trace them back to their high-energy astrophysical origins. One of the most useful physical processes for reconstructing gamma ray directions and energies is gamma-ray pair production. When a high-energy gamma ray interacts with an atomic nucleus, it undergoes a process in which an electron-positron pair is produced. The pair production process is represented in Equation 1.9, where γ represents the gamma ray, e^- represents the electron, and e^+ represents the positron.

$$\gamma \rightarrow e^- + e^+ \tag{1.9}$$

For pair production to occur, the energy of the gamma ray E_γ must be greater than or equal to the combined rest mass energies of the electron E_{e^-} and the positron E_{e^+} by the Law of Conservation of Energy.

$$E_\gamma = E_{e^-} + E_{e^+} \tag{1.10}$$

We can relate the energy of the electron and the positron to their masses by Einstein's Equation (Equation 1.8), where m_e is the rest mass of the electron and m_p is the rest mass of the positron.

$$E_\gamma = m_e c^2 + m_p c^2 \tag{1.11}$$

Since the rest mass of an electron is equivalent to the rest mass of a positron, we can express the minimum gamma ray energy required for pair production as two times the rest mass energy of an electron, which is equivalent to 1.022 MeV.

$$E_\gamma = 2m_e c^2 = 1.022 \text{ MeV} \tag{1.12}$$

Since gamma rays produce electromagnetic radiation in the range of 0.5 MeV to 100 TeV, pair production is an optimal tool for high-energy gamma ray detection. There are many detection methods which directly and indirectly utilize the physical process of pair production to reconstruct gamma ray directions and energies. Space-based gamma-ray telescopes utilize pair production from gamma-ray primaries with energies into the GeV range. Imaging air Cherenkov telescopes (IACTs) utilize pair production in Earth's atmosphere to detect the secondary particles of gamma-ray extensive air showers from the ground level using large segmented mirror imaging. And extensive air shower arrays utilize pair production in Earth's atmosphere to detect the secondary particles of gamma-ray extensive air showers from the ground level using arrays of water Cherenkov detectors. Each class of detectors has unique advantages that allow to observe gamma rays across a very large range of energies. In Figure 1.3, we can see the energy sensitivity ranges for a variety of wavelength detectors including space-based telescopes like Fermi-LAT (Section 1.2.1), IACTs like VERITAS (Section 1.2.2), and extensive air shower arrays like HAWC (Section 1.2.3).

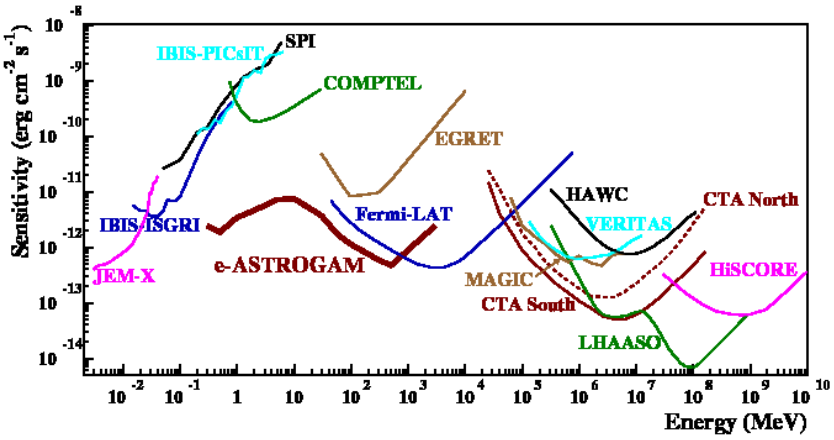

Figure 1.3: Sensitivities of a variety of gamma-ray detectors [11]. We note the sensitivities of Fermi-LAT in dark blue, VERITAS in cyan, and HAWC in black.

1.2.1 Fermi Large Area Telescope

As gamma rays come into contact with Earth's atmosphere, they undergo a pair production process. This causes Earth's atmosphere to be effectively opaque to gamma rays. Space-based gamma-ray telescopes like Fermi-LAT allow us to avoid the complications of pair production from Earth's atmosphere and utilize pair production in a more controlled environment. For this reason, space-based gamma-ray telescopes give us the unique opportunity to detect primary gamma rays.

Located on the Fermi Gamma-Ray Space Telescope in near-earth orbit, the Fermi Large Area Telescope (Fermi-LAT) is a space-based high-energy gamma-ray telescope (Figure 1.4). Fermi-LAT has a nearly continuous duty cycle of $\sim 76\%$, an instantaneous field of view of 2.4 sr with a view of the entire sky every three hours, and an energy range of 20 MeV to 300 GeV [12].

Figure 1.4: An artistic rendering of Fermi-LAT in orbit around Earth [13].

The Fermi-LAT detector, illustrated in Figure 1.5, is made up of 16 towers each consisting of 20 layers of tungsten, 36 layers of silicon, an eight-layer cesium iodide crystal calorimeter, and a plastic tile Anticoincidence Detector (ACD) (see Figure 1.5) [12, 14]. When a primary gamma ray interacts with the tungsten, it undergoes pair production and produces an electron-positron pair. The paths of the charged pair production secondaries are then tracked by the silicon layers and their energies are measured by the calorimeter [12, 14]. Since the silicon serves as a charged particle detector, it also has the ability to detect background events produced by cosmic rays [12]. In order to remove these cosmic ray detections from the data, Fermi-LAT is equipped with an ACD. When charged cosmic rays hit the ACD, they interact with specially formulated plastic tiles and produce flashes of light [14]. Detection of these flashes allows for the distinction of charged gamma-ray pair production secondaries from charged cosmic rays. From the energies of gamma-ray secondaries and their paths, Fermi-LAT is able to determine the energies of gamma-ray primaries and trace them back to their high-energy origins.

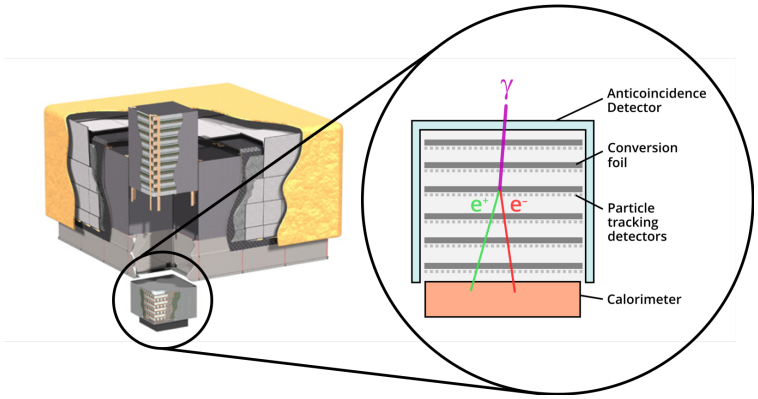

Figure 1.5: An artist's rendition of the inside of the Fermi-LAT Detector (left) [15]. A zoomed in image of the tungsten and silicon layers with the calorimeter at the bottom (right) [14].

Although Fermi-LAT and other space-based gamma-ray telescopes have the unique advantage of avoiding the effective gamma ray opaqueness of Earth's atmosphere, their small effective areas prohibit them from detecting VHE gamma rays. Since VHE gamma rays have low flux, their detection requires an extremely large detector area. This type of large area detector is only plausible from the ground. This leads us into the discussions of ground-based IACTs and extensive air shower arrays.

1.2.2 Very Energetic Radiation Imaging Telescope Array System

Located at the Fred Lawrence Whipple Observatory (FLWO) in southern Arizona, The Very Energetic Radiation Imaging Telescope Array System (VERITAS) is a ground-based IACT, which detects light from particle showers in the atmosphere [16]. VERITAS has an angular resolution of 0.08° at 1 TeV and 0.13° at 200 GeV, a field of view of $\sim 3.5°$, and high sensitivity in the energy range of 50 GeV to 50 TeV. VERITAS operates best for point-like sources with declinations between 0° and 60°. Contrary to Fermi-LAT, VERITAS has a very limited duty cycle. Due to the nature of the detection methods, VERITAS only observes under clear, dark skies and does not observe during the summer due to local weather conditions.

Figure 1.6: The four 12-meter Cherenkov telescopes that comprise VERITAS (left) [17]. Close-up of one of VERITAS's four Cherenkov telescopes with 350 hexagonal spherical mirrors (right) [18].

While Fermi-LAT directly detects the primary gamma rays produced by astrophysical accelerators, VERITAS detects the secondary particles produced when a primary gamma ray interacts with Earth's atmosphere and undergoes pair production. When atmospheric pair production occurs, an extensive air shower of secondary particles is created (see Figure 1.7, left).

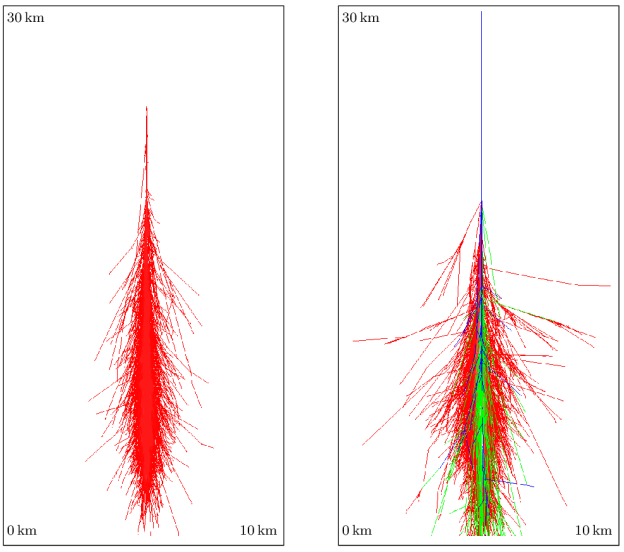

Figure 1.7: A gamma-ray extensive air shower model (left) and a cosmic-ray extensive air shower model (right). The red lines represent gamma rays, electrons, and positrons, the blue lines represent hadrons, and the green lines represent muons. [19]

VERITAS, pictured in Figure 1.6, is made up of four 12-meter Cherenkov telescopes. Each of these four telescopes has 350 hexagonal spherical mirrors [20]. These telescopes are designed to detect a special type of light called Cherenkov radiation. Just as a sonic boom is created by an object traveling through air faster than the speed of sound in air, nanosecond bursts of Cherenkov radiation are produced by high-energy gamma rays darting through the dark sky faster than the speed of light in air. When Cherenkov radiation hits the mirrors, it is focused towards a camera composed of 1000 photomultiplier tubes [20]. These cameras then produce images of the Cherenkov radiation, which VERITAS utilizes to reconstruct extensive air showers. Due to the differences in shape and particle secondaries produced by gamma-ray and cosmic-ray extensive air showers (see Figure 1.7), VERITAS is able to remove cosmic ray data and trace gamma-ray showers back to their high-energy origins.

1.2.3 High Altitude Water Cherenkov Gamma-Ray Observatory

Located in Puebla, Mexico, the High Altitude Water Cherenkov (HAWC) Observatory (Figure 1.8) is currently one of the most sensitive VHE gamma-ray detectors [21]. HAWC is an extensive air shower array that detects gamma rays from the ground level [22]. Collecting data with an air shower array increases the duty cycle, field of view, and energy threshold compared to IACTs like VERITAS. HAWC has an angular resolutuon of 0.01°, a duty cycle of $> 95\%$, an instantaneous field of view of 2 sr, and an energy range of 100 GeV to 100 TeV [21]. HAWC observes high-energy gamma-ray sources with declinations between $-20°$ and $60°$ [4]. These advantages allow HAWC to operate during all weather conditions and view two thirds of the sky during each 24 hour period [21].

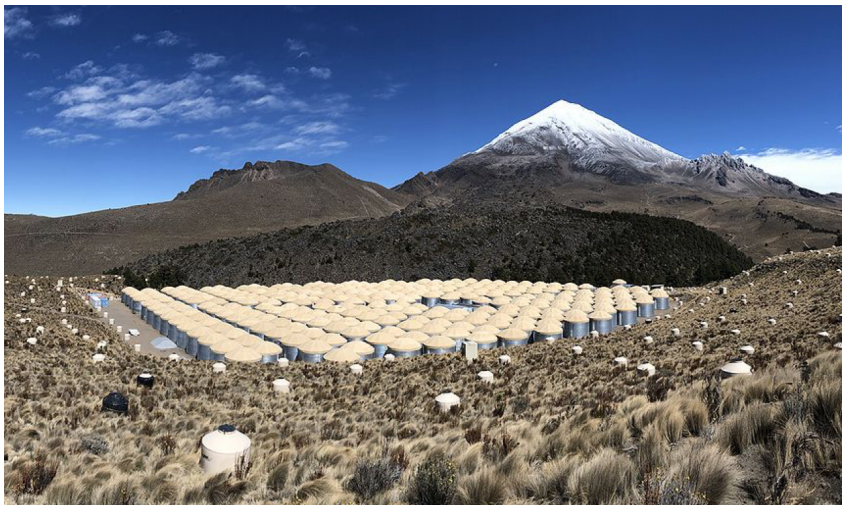

Figure 1.8: The High Altitude Water Cherenkov (HAWC) Observatory located near Puebla, Mexico [3].

Similarly to VERITAS, HAWC relies on the reconstruction of extensive air showers produced by the interaction of gamma rays with Earth's atmosphere. As the secondary particles from the extensive air shower wash over HAWC's array of detectors, the shape and direction of the shower is reconstructed and the arrival direction of the gamma-ray primary is determined.

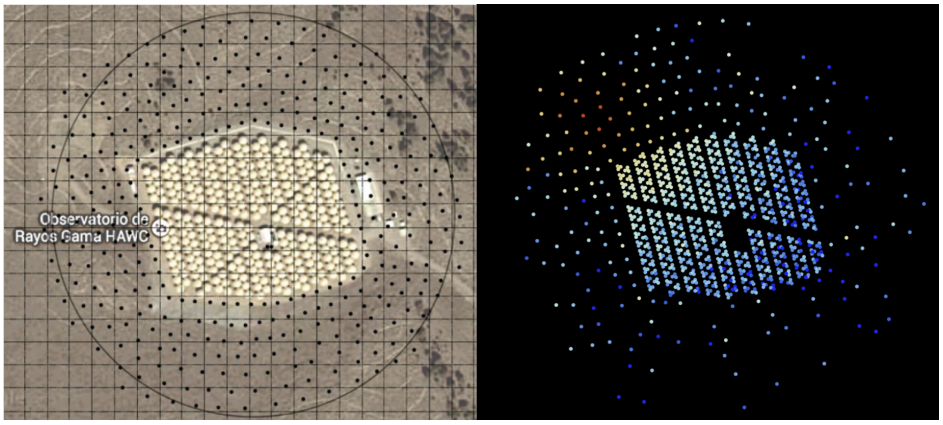

Figure 1.9: HAWC site with the array in the center and outriggers in black (left) [23]. A gamma ray simulation of a single event shower across HAWC (right) [24].

The HAWC array, illustrated in Figure 1.9, is made up of 300 Water Cherenkov Detectors (WCDs). WCDs are large steel tanks filled with purified water and covered with light-blocking domes. Each WCDs has four photomultiplier tubes/photosensors affixed to the bottom (see Figure 1.10). When fast-moving gamma rays enter the WCDs, they produce electron-positron pairs. These relativistic charged electrons and positrons travel through water faster than the speed of light in water and produce Cherenkov radiation. When Cherenkov radiation is produced, it is detected by the photomultiplier tubes, and its arrival time is recorded [22]. As soon as HAWC registers an event, it is able to establish parameters such as the direction and size of the air shower [22]. Although the main purpose of HAWC is to take advantage of the uninhibited paths of neutrally

charged gamma rays, a large portion of the particles detected originate from cosmic-ray showers [25]. Due to randomized magnetic deflection, cosmic rays produce a relatively uniform background. This background is removed from the data using the direct integration method [25, 26].

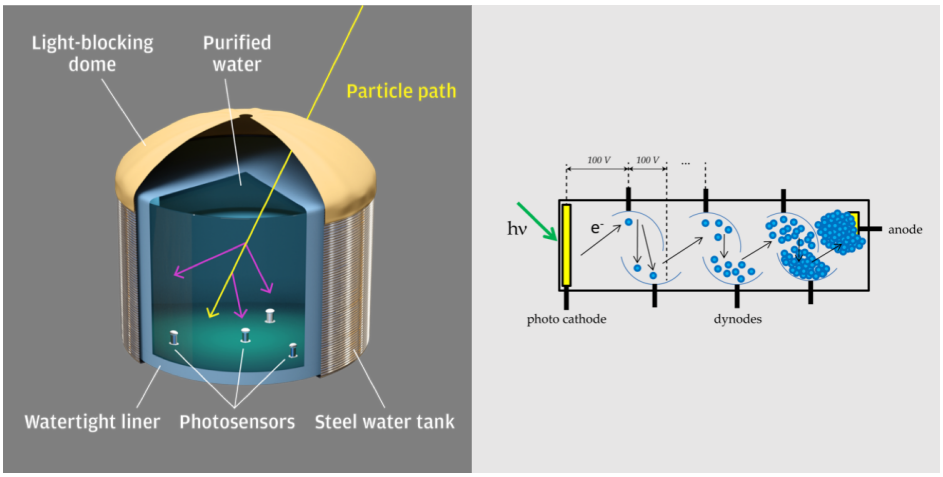

Figure 1.10: Representation of a relativistic charged particle emitting Cherenkov radiation as it moves through water in one of the HAWC water Cherenkov detectors (left) [27]. The path of the charged particle is represented by the yellow line while the Cherenkov radiation is represented by pink lines [3]. Each Water Cherenkov Detector is filled with purified water and contains four photomultiplier tubes or photosensors. Representation of a photomultiplier tube or photosensor (right) [28].

CHAPTER2

Methods

2.1 Initial Blind Search: The 2HWC Catalog

With HAWC's wide field of view and large duty cycle, we are able to conduct "blind searches" for TeV gamma-ray excesses. In 2017, HAWC performed a blind search with 508 days of observations, and released the 2HWC catalog [4]. For this blind search, we considered three different basic morphological models- a point source model, a 0.5° extended source model, and a 1.0° extended source model. We define a source or candidate source as an excess when the Test Statistic (TS) (Equation 2.2) surpasses a threshold of 25. If an excess first passed the TS threshold with a point source assumption it was classified as a point source, if an excess first passed the TS threshold with a 0.5° extended source assumption it was classified as a 0.5° extended source, and if an excess first passed the TS threshold with a 1.0° extended source assumption it was classified as a 1.0° extended source [4]. For this reason, the morphological designations presented in the 2HWC catalog are not necessarily accurate and require more detailed study. This is especially the case for unidentified excesses.

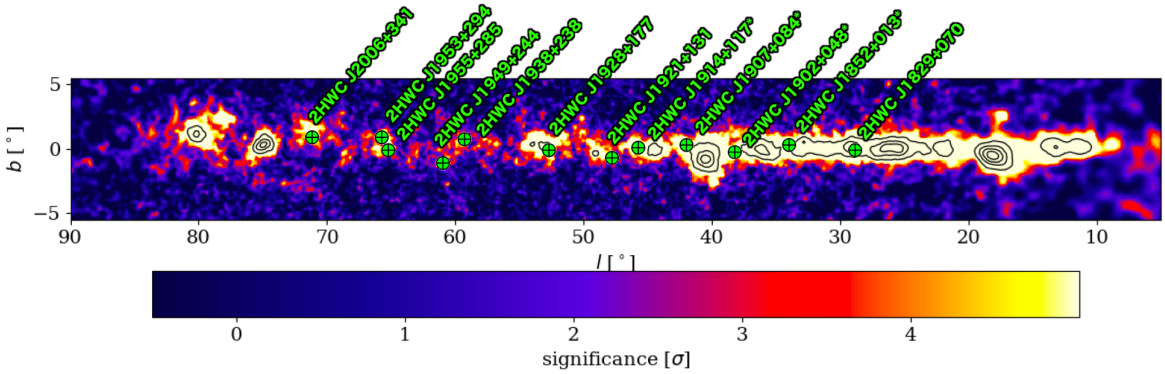

Figure 2.1: HAWC's view of the Galactic Plane, including 12 of the 16 unassociated candidate TeV sources. (Contour lines at 10σ, 20σ, 30σ, and 40σ).

In this blind search, we pinpointed 23 excesses with no clear identification, 16 of which were $\geq 1°$ away from known TeV sources [4]. We labeled these 16 excesses in the VHE gamma-ray sky as *unassociated candidate TeV sources*. In this work, we investigate these 16 unassociated candidate TeV sources with a total of 1523 days of observations. With these new data, we update the

locations of the candidate sources and reevaluate their extensions. We carry out an analysis of the temporal progression of the statistical significance and flux of these TeV candidates to determine if they have faded into the diffuse gamma radiation or if they can still be considered considered unassociated candidate TeV sources. We compare our results to those published in the newest HAWC blind search which is referred to as the 3HWC catalog [5]. In addition, we perform preliminary morphological and spectral fits for some of the candidate sources (see the Appendix).

2.2 Temporal Progression of The Excesses

2.2.1 Significance Progression

We characterize the number of standard deviations σ in our data as the significance, which is equivalent to the square root of the test statistic TS [29].

$$\sigma = \sqrt{\text{TS}} \tag{2.1}$$

In order to determine the significance of a candidate source, we perform a likelihood analysis using a test statistic. We express the relationship between the test statistic and the likelihood in Equation 2.2 [29], where $\mathcal{L}^{max}(\text{Source Model})$ is the sum of the source counts and background model counts for all pixels in a region of interest and $\mathcal{L}(\text{Null Hypothesis})$ is the expected counts based on the background model only [4, 29]. We estimate the background counts based on the direct integration method [30].

$$\text{TS} = 2\ln\left[\frac{\mathcal{L}^{max}(\text{Source Model})}{\mathcal{L}(\text{Null Hypothesis})}\right] \tag{2.2}$$

Wilks' Theorem asserts that "the distribution of the test statistic asymptotically approaches a χ^2 distribution under the null hypothesis" [31]. Thus, HAWC's large number of events allows us to approximate the distribution of the test statistic as a χ^2 distribution [32]. Since a χ^2 distribution reaches a confidence level of ∼99.99884% at 5 standard deviations [32], we qualify an excess as a source candidate once its significance reaches a threshold of 5 (when its TS reaches a threshold of 25) [4]. Further, we designate a source candidate as *primary* if it has a "TS valley" dip of $\Delta\text{TS} > 2$ between any neighboring source(s) and *secondary* if it has a "TS valley" dip of $1 < \Delta\text{TS} < 2$ between any neighboring source(s).

For each of the 16 unassociated sources in the 2HWC catalog, we analyzed the significance progression using the Analysis and Event Reconstruction Integrated Environment (AERIE) framework designed specifically for the analysis of HAWC data [33]. We examined their significance with 508 days of observations to confirm values reported in the 2HWC catalog [4]. We then examined the significance of each source with increasing amounts of cumulative data. We expect the significance of a true source to increase with additional data. The expected progression of a source's significance over a period of time follows the relationship expressed by Equation 2.3, where σ_{old} is the significance with an initial dataset, σ_{new} is the significance of a newer dataset, and t_{old} and t_{new} are the duration of the initial observation period and the duration of the newer data observation period, respectively.

$$\sigma_{new} = \sigma_{old}\sqrt{\frac{t_{new}}{t_{old}}}, \tag{2.3}$$

For example, if a source had a significance of σ_{old} in the initial dataset of 508 days of observations, we would expect it to have a significance of $1.73\sigma_{old}$ in the newest dataset of 1523 days of observations. In order to examine source candidates, we create significance maps which assume a power law spectrum with an index of -2.5 [29]. In Figure 2.2 we present the significance progression for the Crab Nebula as a reference point. As we can see in Table 2.1, the significance progresses as we would expect it to based on Equation 2.3.

Observation Period	Actual Significance	Expected Significance	Percent Error
508 Days	105	-	-
1132 Days	161	157	3
1523 Days	189	187	1

Table 2.1: The actual significance progression versus the expected significance progression for the Crab Nebula for three cumulative observation periods. The expected significance for 1132 days of observations was computed based on the actual significance for 508 days of observations and the expected significance for 1523 days of observations was computed based on the actual significance for 1132 days of observations (see Equation 2.3). The Percent Error between the actual significance and the expected significance was computed using Equation 2.4.

$$\text{Percent Error} = \frac{|\text{Actual} - \text{Expected}|}{\text{Actual}} \times 100 \tag{2.4}$$

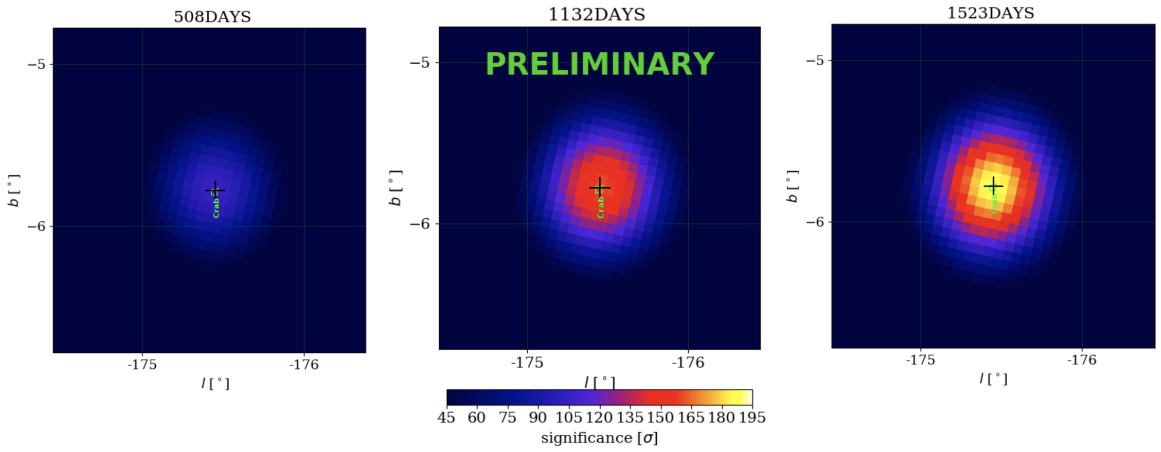

Figure 2.2: Three maps of HAWC data for the Crab Nebula with 508 cumulative days of data (left), 1132 cumulative days of data (center), and 1523 cumulative days of data (right). The vertical axes show galactic latitude in degrees, while the horizontal axes show galactic longitude in degrees. The color scale indicates the significance of the source.

2.2.2 Epoch Examination

In addition, we used AERIE to examine the flux and significance of each source over independent epochs with approximately the same amount of observation time [33]. For a true TeV source, we expect to see fairly consistent flux and significance among the epochs. Evaluating the flux and significance in this way allowed us to uncover any inconsistencies in the source during a specific epoch, which could be attributed to fluctuations in the background rather than a TeV source. In order to perform this analysis, we split the data collected over 1523 days of observations into three independent epochs; Epoch 1 comprising data from the first ∼503 days of observations, Epoch 2 comprising data from the next ∼514 days of observations, and Epoch 3 comprising data from the next ∼506 days of observations. In Figure 2.3 we present the epoch examination for the Crab Nebula as a reference point. As we can see in Table 2.2, the flux and significance remain consistent. The Crab Nebula serves as a standard example of our expectations for a true TeV steady source.

Observation Period	Significance	Flux (TeV^{-1} cm^{-2} s^{-1})
Epoch 1	104	2.13 ± 0.03 E-13
Epoch 2	114	2.38 ± 0.02 E-13
Epoch 3	109	2.30 ± 0.02 E-13

Table 2.2: The significance and flux for the Crab Nebula modeled as a point source in 3 separate epochs each with an observation period of ∼508 days.

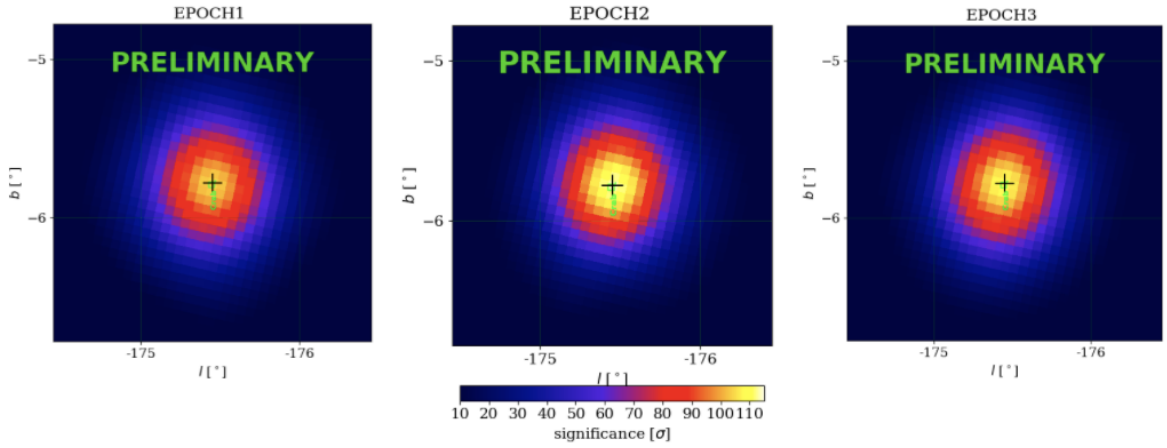

Figure 2.3: Three maps of HAWC data for the Crab Nebula in Epoch 1 (left), Epoch 2 (center), and Epoch 3 (right). The vertical axes show galactic latitude in degrees, while the horizontal axes show galactic longitude in degrees. The color scale indicates the significance of the source.

2.3 Source Morphology

In order to determine the updated location and extension of a candidate source, we fit its location of maximum significance with morphological assumptions using AERIE, The Multi-Mission

Maximum Likelihood Framework (3ML), and the HAWC Accelerated Likelihood (HAL) plugin [33, 34]. For the initial location fits, we assumed a spectral index of -2.5, a pivot energy of 7 TeV, and a double-Gaussian model. We classify a point source as a source whose diameter is smaller than the point spread function of the detector. On the contrary, we classify a source as extended if its radius is larger than the point response of the detector [3]. When we model a source with an extended map, we may experience an overlap in data from nearby sources that have lower extensions [4]. If this effect is not taken into consideration, a source modeled with larger extension may appear to be more significant than it is. In order to minimize this effect, we carefully consider the significance as well as the local environment when we examine the extension of a source.

2.4 Spectral Energy Distributions

Generally, we can describe the spectral energy distributions of VHE gamma-ray sources with simple power laws [2]. A power law can be expressed as

$$dN/dE = F_0(E/E_0)^{\alpha}, \tag{2.5}$$

where dN/dE is the differential flux, F_0 is the differential flux at the pivot energy, E is the energy, E_0 is the pivot energy, and α is the spectral index. The pivot energy represents the optimal energy for minimizing the correlation between flux and spectral index. In most cases, we assume a pivot energy of 7 TeV, which is the optimal value for the Crab Nebula [25]. In more complex cases, other models are used. For example, a power law with a cutoff can be expressed as

$$dN/dE = F_0(E/E_0)^{\alpha}\exp(-E/E_c), \tag{2.6}$$

where E_c is the cutoff energy. Another commonly used expression is the log parabola relationship

$$dN/dE = F_0(E/E_0)^{\alpha+\beta\log(E/E_0)}, \tag{2.7}$$

where β is the secondary spectral index. In Figure 2.4, we present the spectral fit for the Crab Nebula performed with HAWC data. If more data becomes available for these candidate sources in the future, we may be able to fit their spectra to more specific models such as the cutoff power law or log parabola. For this reason, we only present preliminary spectral energy distributions for a few selected sources that were studied in greater detail (see the Appendix).

In order to create a spectral energy distribution, we organize our data into 2D bins based on shower size (see Table 4.1 in the Appendix) and energy (see Table 4.2 in the Appendix). This 2D binning scheme is necessary because the angular resolution of HAWC varies based on both the size and energy of a shower [35]. In addition, the energy of a shower is heavily dependent on its zenith angle. Therefore, we take into account the difference in energy distribution caused by differences in source declination [35, 22, 36]. Moreover, we remove GeV energy bins because the bias is larger than the energy resolution in this energy range, and we remove bins with poor point spread functions [35]. (For specifications on 2D binning schemes for given source declination, please see Tables 4.3 in the Appendix [36].) For this analysis, we carry out all of our fits using The Multi-Mission Maximum Likelihood Framework (3ML) and the HAWC Accelerated Likelihood (HAL) plugin [34]. Since we have very limited data for these unidentified candidate TeV sources,

we were only able to fit very preliminary spectra. Source for which we were able to fit preliminary spectra are presented in the Appendix.

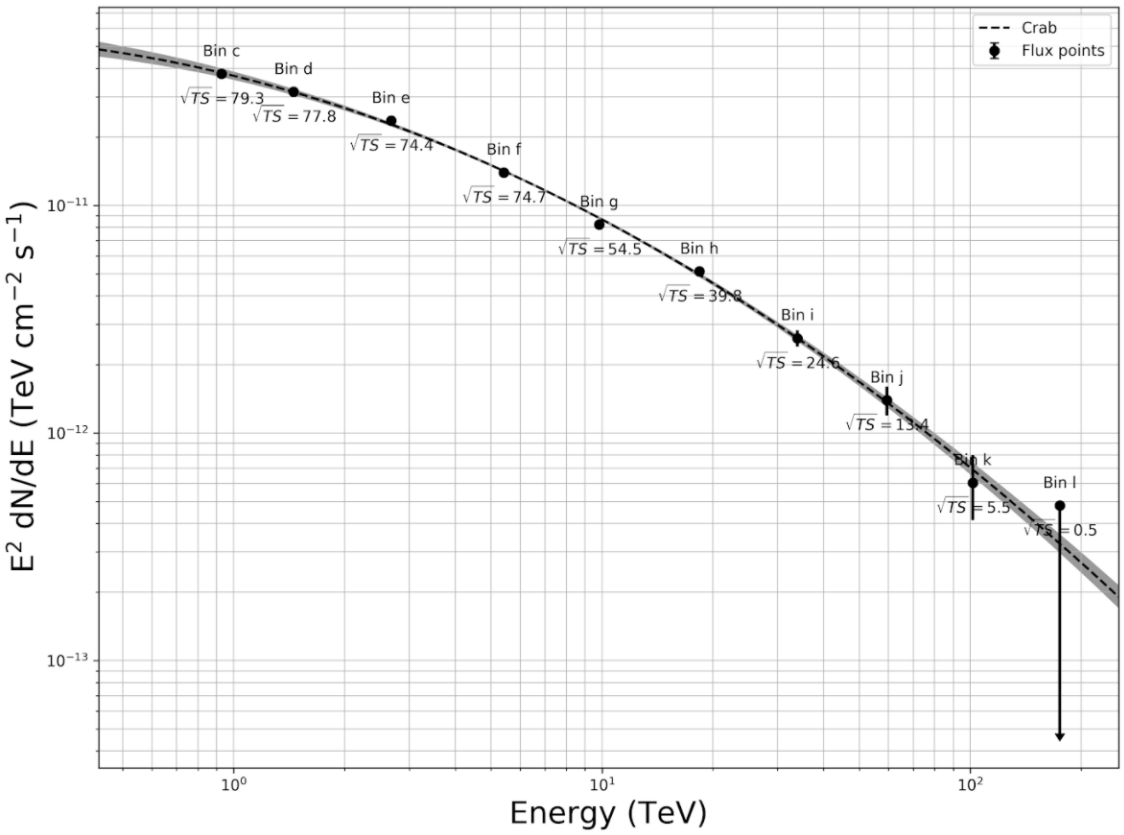

Figure 2.4: Spectral energy distribution of HAWC data for the Crab Nebula fit to a log parabola using 3ML.

CHAPTER3

Results

In this chapter we discuss each of the 16 excesses detected in the 2HWC catalog in detail. The excesses that remain candidate TeV sources are presented in the *New TeV Sources* section and the excesses that are no longer considered candidate TeV sources are presented in the *Other Sources* section. For all of the significance progression data presented in this chapter, the expected significance for 1132 days of data was computed based on the actual significance for 508 days of data, and the expected significance for 1523 days of data was computed based on the actual significance for 1132 days of data (see Equation 2.3). The Percent Error between the actual significance and the expected significance was computed using Equation 2.4. All secondary sources from the 2HWC catalog are marked with an asterisk (*) and all secondary sources from the 3HWC catalog are marked with an dagger (†).

3.1 New TeV Sources

3.1.1 2HWC J0700+143

2HWC J0700+143 was classified as a 1.0° extended source in the 2HWC catalog [4]. We update the location of maximum significance from $l = 201.10^\circ$, $b = 8.44^\circ$ [4] to $l = 200.87^\circ$, $b = 8.32^\circ$. The updated location is 0.23° from the original location, which falls into the location uncertainty of 0.80° reported in the 2HWC catalog [4]. Examining the temporal progression of this excess at the updated location, we conclude that 2HWC J0700+143 remains a candidate TeV source. This excess is present in the 3HWC catalog as the two point sources 3HWC J0659+147† and 3HWC J0702+147, where 3HWC J0659+147† only passes the secondary source TS criteria because it is not separated from nearby sources with a large TS gap [5]. However, these two detection can likely be attributed to the complex morphology of the extended source [5].

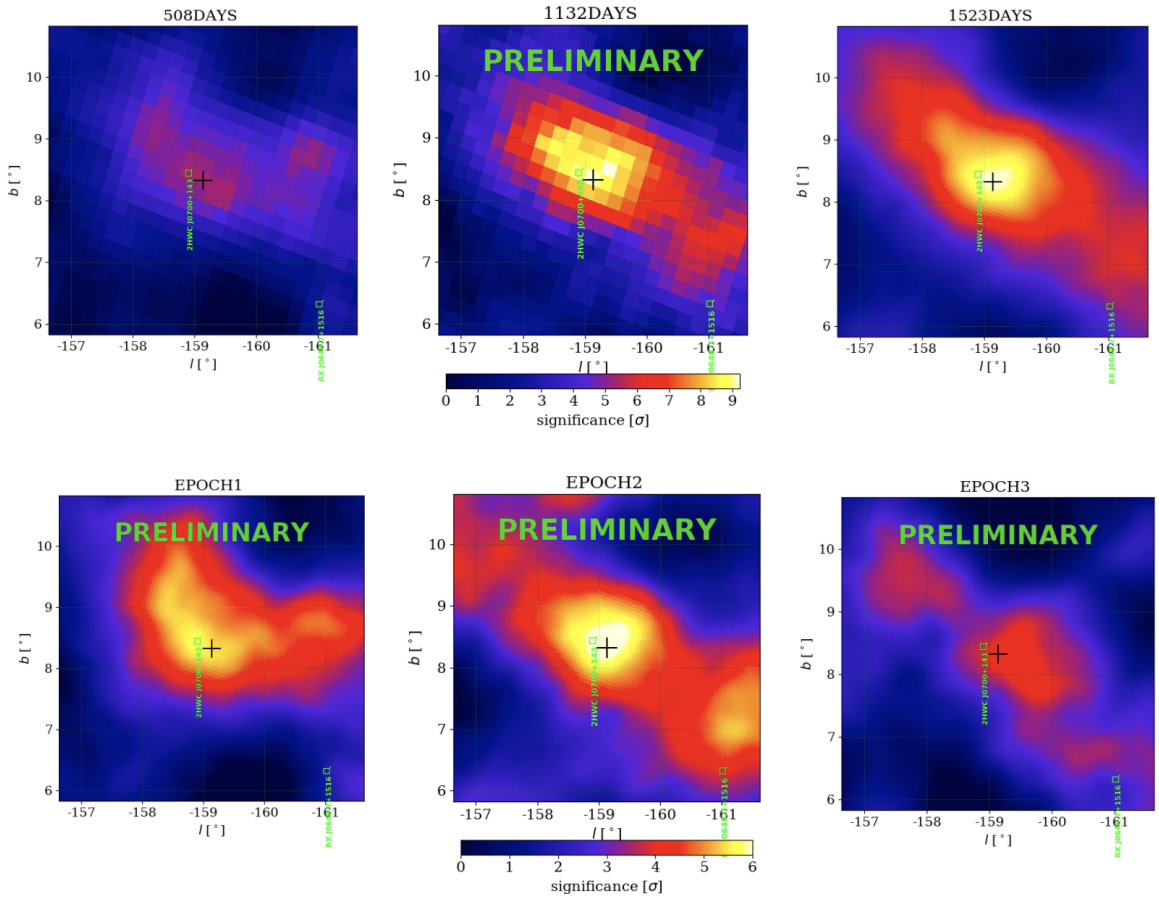

Figure 3.1: Three 1.0° extended source maps of cumulative HAWC data for 508 days of data (top left), 1132 days of data (top center), and 1523 days of data (top right). Three 1.0° extended source maps of HAWC data of 2HWC J0700+143 in Epoch 1 (bottom left), Epoch 2 (bottom center), and Epoch 3 (bottom right). The vertical axes show galactic latitude in degrees, while the horizontal axes show galactic longitude in degrees. The color scale indicates the significance of the source. The square is the source location based on the 2HWC catalog, the cross is the updated location.

Observation Period	Actual Significance	Expected Significance	Percent Error
508 Days	5.4	-	-
1132 Days	9.1	8.1	13.4
1523 Days	9.2	10.6	12.9

Table 3.1: The significance progression for 2HWC J0700+143 at the updated location modeled as a 1.0° extended source for three cumulative observation periods.

Epoch	Significance	Flux ($\text{TeV}^{-1}\text{cm}^{-2}\text{s}^{-1}$)
1	5.7	3.0 ± 0.5 E-12
2	6.3	3.3 ± 0.5 E-12
3	4.0	2.1 ± 0.5 E-13

Table 3.2: The significance and flux for 2HWC J0700+143 at the updated location modeled as a 1.0° extended source in 3 separate epochs each with an observation period of $\sim$508 days.

3.1.2 2HWC J1852+013*

2HWC J1852+013* was classified as a point source in the 2HWC catalog [4]. We update the location of maximum significance from $l = 34.23^\circ$, $b = 0.50^\circ$ [4] to $l = 34.21^\circ$, $b = 0.45^\circ$. The updated location is 0.05° from the original location, which falls into the location uncertainty of 0.13° reported in the 2HWC catalog [4]. Examining the temporal progression of this excess at the updated location of maximum significance, we conclude that 2HWC J1852+013* remains a candidate TeV source. However, 2HWC J1852+013* only passes the secondary source TS criteria because it is not separated from nearby sources with a large TS gap. This excess is present in the 3HWC catalog as the point source 3HWC J1852+013† [5].

2HWC J1852+013* resides in a very complex region which presents many challenges for our morphological investigations. The region directly surrounding 2HWC J1852+013* contains four slightly extended TeV sources; HESS J1857+026, HESS J1858+020, HESS J1852-000, and HESS J1849-000 (see Figure 3.3). In order to minimize contamination from these nearby sources, morphological studies of the 2HWC J1852+013* region will require more robust methods in which nearby sources can be removed from the model.

Observation Period	Actual Significance	Expected Significance	Percent Error
508 Days	8.3	-	-
1132 Days	10.6	12.3	13.7
1523 Days	11.3	12.3	8.8

Table 3.3: The significance progression for 2HWC J1852+013* at the updated location modeled as a point source for three cumulative observation periods.

Epoch	Significance	Flux ($TeV^{-1}cm^{-2}s^{-1}$)
1	8.6	2.5 ± 0.3E-12
2	6.0	1.7 ± 0.3E-12
3	7.3	2.0 ± 0.3E-12

Table 3.4: The significance and flux for 2HWC J1852+013* at the updated location modeled as a point source in 3 separate epochs each with an observation period of ∼508 days.

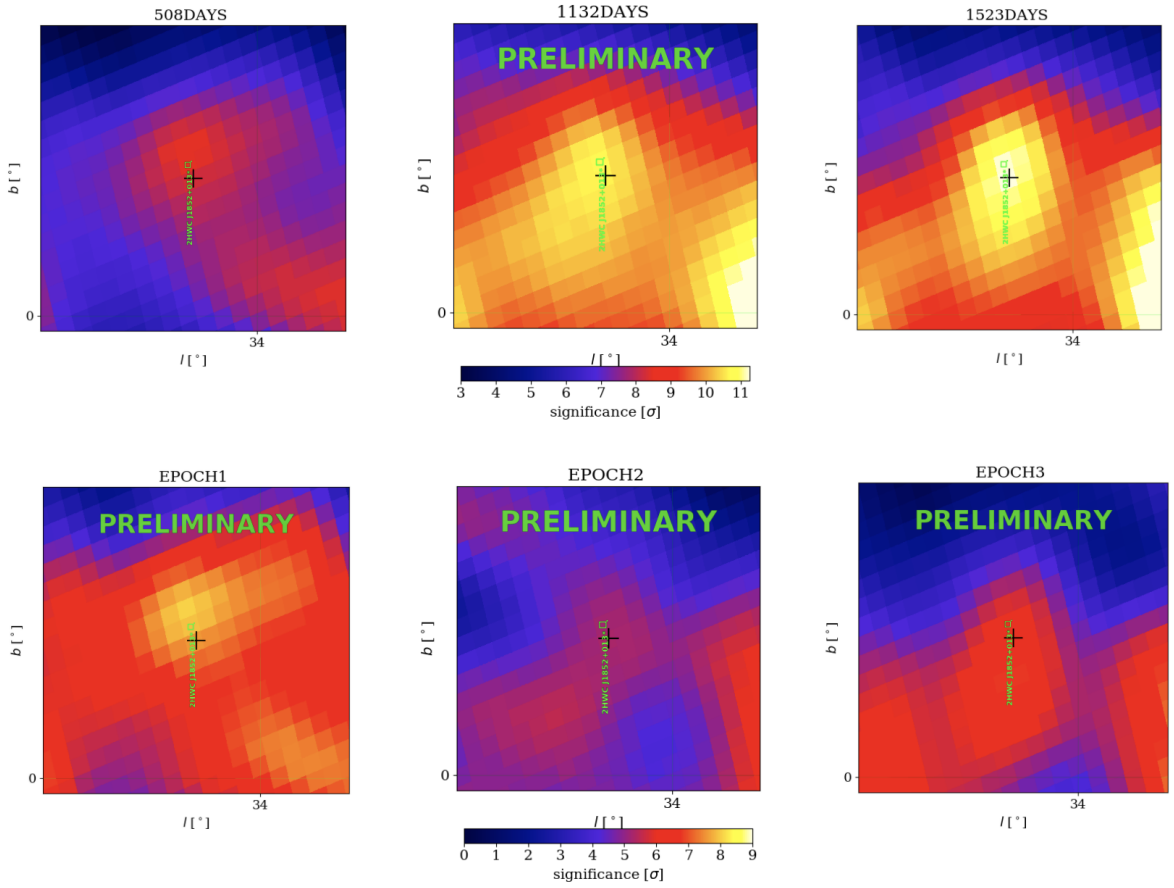

Figure 3.2: Three point source maps of cumulative HAWC data for 2HWC J1852+013* for 508 days of data (top left), 1132 days of data (top center), and 1523 days of data (top right). Three point source maps of HAWC data of 2HWC J1852+013* in Epoch 1 (bottom left), Epoch 2 (bottom center), and Epoch 3 (bottom right). The vertical axes show galactic latitude in degrees, while the horizontal axes show galactic longitude in degrees. The color scale indicates the significance of the source. The square is the source location based on the 2HWC catalog, the cross is the updated location.

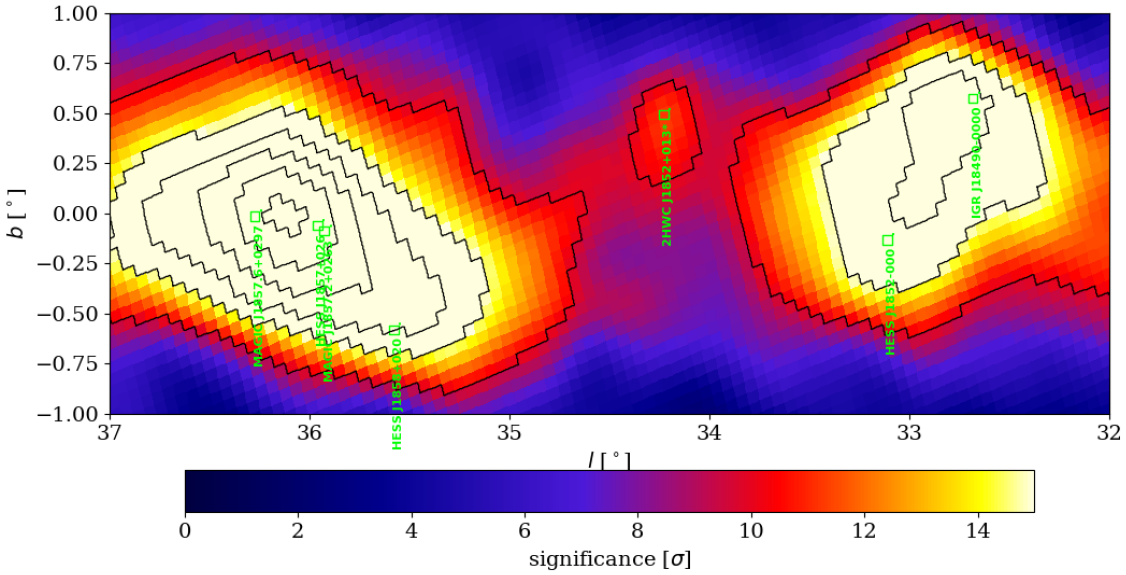

Figure 3.3: Point Source Map using 1523 days of HAWC data in the region around 2HWC J1852+013* with contour lines representing 6.5σ, 7.0σ, and 7.5σ.

3.1.3 2HWC J1907+084*

2HWC J1907+084* was classified as a point source in the 2HWC catalog [4]. We update the location of maximum significance from $l = 42.28°$, $b = 0.41°$ [4] to $l = 42.34°$, $b = 0.44°$. The updated location is $0.07°$ from the original location, which falls into the location uncertainty of $0.27°$ reported in the 2HWC catalog [4]. Examining the temporal progression of this excess at the updated location of maximum significance, we conclude that 2HWC J1907+084* remains a candidate TeV source, unassociated with the nearby source W 49B and the extended source MGRO J1908+06. This excess is present in the 3HWC catalog as the point source 3HWC J1907+085 [5].

Observation Period	Actual Significance	Expected Significance	Percent Error
508 Days	5.7	-	-
1132 Days	7.8	8.5	8.3
1523 Days	8.7	9.1	4.0

Table 3.5: The significance progression for 2HWC J1907+084* at the updated location modeled as a point source for three cumulative observation periods.

Epoch	Significance	Flux ($TeV^{-1}cm^{-2}s^{-1}$)
1	5.2	1.2 ± 0.3 E-12
2	5.6	1.3 ± 0.3 E-12
3	6.0	1.4 ± 0.3 E-12

Table 3.6: The significance and flux for 2HWC J1907+084* at the updated location modeled as a point source in 3 separate epochs each with an observation period of ∼508 days.

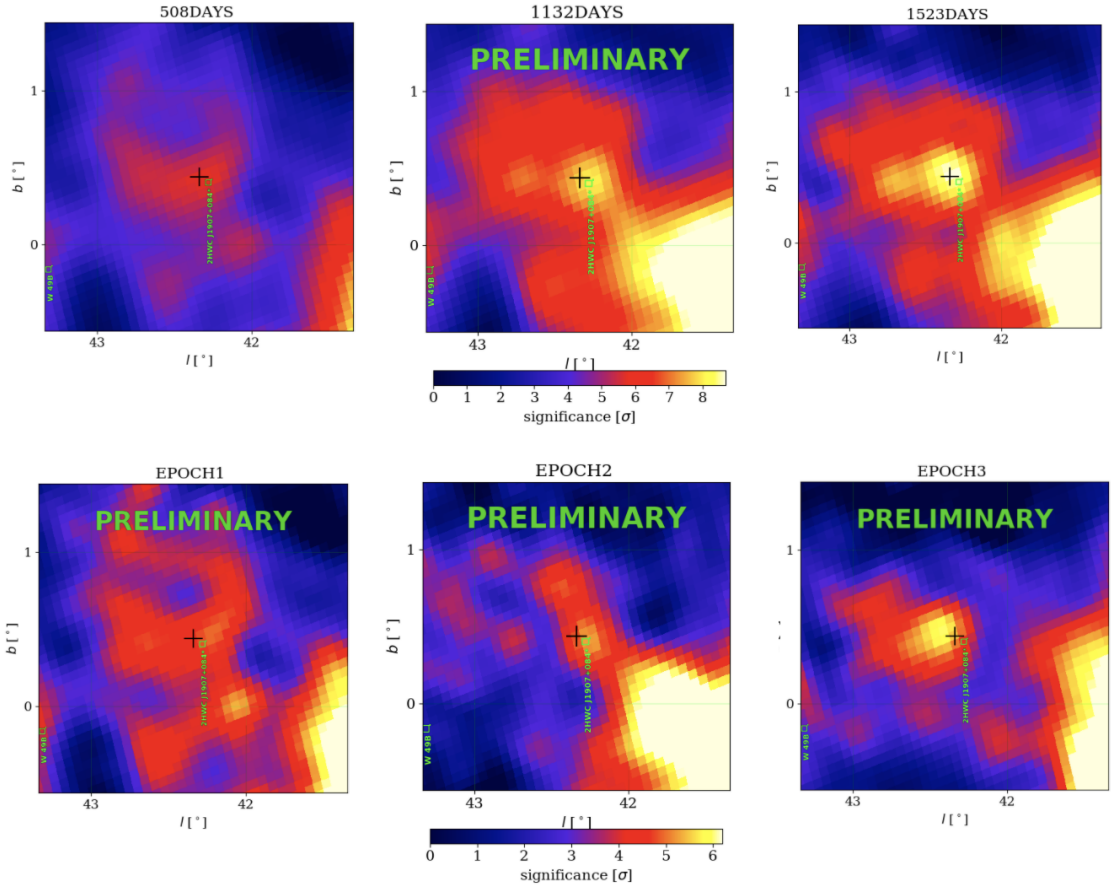

Figure 3.4: Three point source maps of cumulative HAWC data for 2HWC J1907+084* for 508 days of data (top left), 1132 days of data (top center), and 1523 days of data (top right). Three point source maps of HAWC data of 2HWC J1907+084* in Epoch 1 (bottom left), Epoch 2 (bottom center), and Epoch 3 (bottom right). The vertical axes show galactic latitude in degrees, while the horizontal axes show galactic longitude in degrees. The color scale indicates the significance of the source. The square is the source location based on the 2HWC catalog, the cross is the updated location.

3.1.4 2HWC J1914+117*

2HWC J1914+117* was classified as a point source in the 2HWC catalog [4]. We update the location of maximum significance from $l = 46.00°$, $b = 0.25°$ [4] to $l = 46.13°$, $b = 0.32°$. The updated location is $0.15°$ from the original location, which is comparable to the location uncertainty of $0.13°$ reported in the 2HWC catalog [4]. Examining the temporal progression of this excess at the updated location of maximum significance, we conclude that 2HWC J1914+117* remains a candidate TeV source. This excess is present in the 3HWC catalog as the point source 3HWC J1914+118 [5].

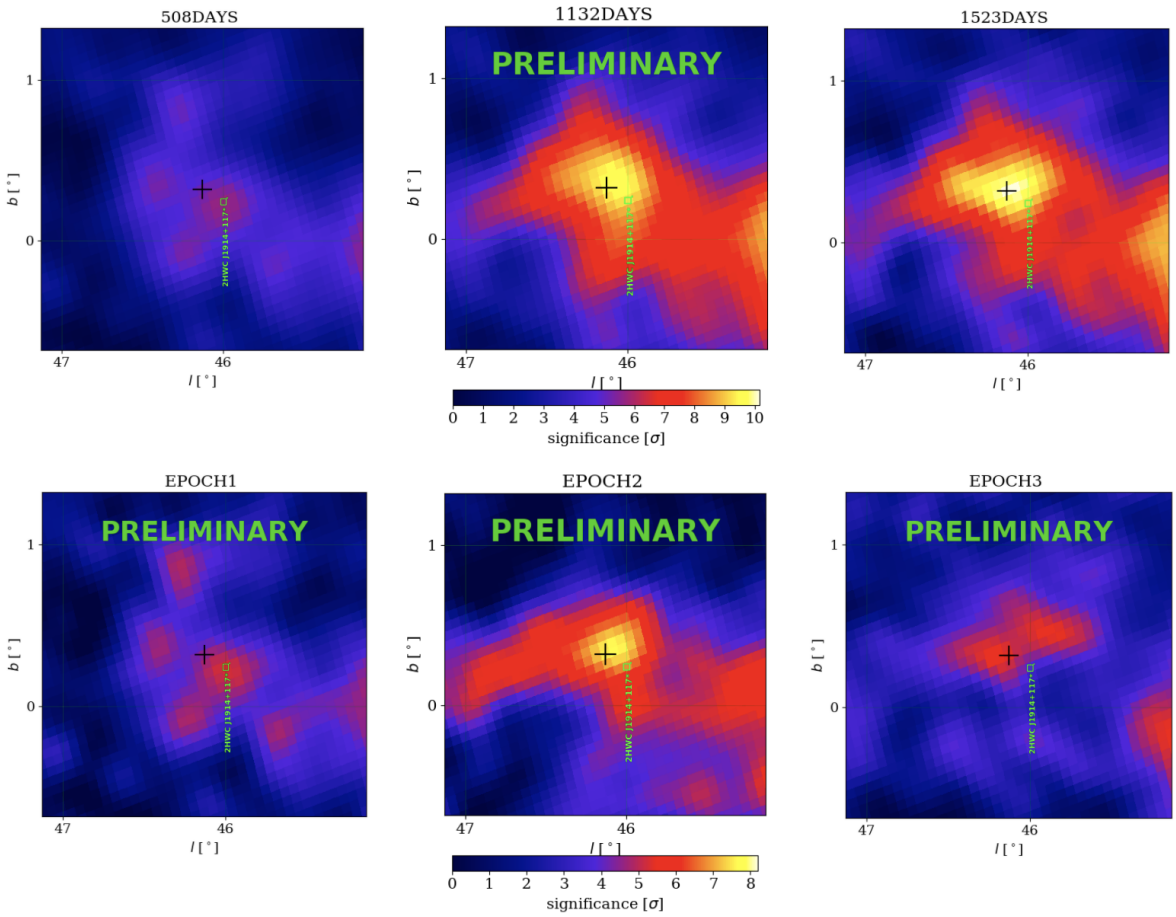

Figure 3.5: Three point source maps of cumulative HAWC data for 2HWC J1914+117* for 508 days of data (top left), 1132 days of data (top center), and 1523 days of data (top right). Three point source maps of HAWC data of 2HWC J1914+117* in Epoch 1 (bottom left), Epoch 2 (bottom center), and Epoch 3 (bottom right). The vertical axes show galactic latitude in degrees, while the horizontal axes show galactic longitude in degrees. The color scale indicates the significance of the source. The square is the source location based on the 2HWC catalog, the cross is the updated location.

Observation Period	Actual Significance	Expected Significance	Percent Error
508 Days	5.2	-	-
1132 Days	9.6	7.7	23.6
1523 Days	10.2	11.1	8.5

Table 3.7: The significance progression for 2HWC J1914+117* at the updated location modeled as a point source for three cumulative observation periods.

Epoch	Significance	Flux ($\text{TeV}^{-1}\text{cm}^{-2}\text{s}^{-1}$)
1	5.0	1.1 ± 0.2 E-12
2	8.1	1.9 ± 0.3 E-12
3	6.0	1.3 ± 0.2 E-12

Table 3.8: The significance and flux for 2HWC J1914+117* at the updated location modeled as a point source in 3 separate epochs each with an observation period of $\sim$508 days.

3.1.5 2HWC J1928+177

2HWC J1928+177 was classified as a point source in the 2HWC catalog [4]. We update the location of maximum significance from $l = 52.92°$, $b = 0.14°$ [4] to $l = 52.94°$, $b = 0.20°$. The updated location is $0.06°$ from the original location, which falls within the location uncertainty of $0.07°$ reported in the 2HWC catalog [4]. Examining the temporal progression of this excess at the updated location of maximum significance, we conclude that 2HWC J1928+177 remains a candidate TeV source. This excess is present in the 3HWC catalog as the point source 3HWC J1928+178 [5].

Observation Period	Actual Significance	Expected Significance	Percent Error
508 Days	7.9	-	-
1132 Days	12.4	11.8	4.6
1523 Days	14.7	14.4	2.5

Table 3.9: The significance progression for 2HWC J1928+177 at the updated location modeled as a point source for three cumulative observation periods.

Epoch	Significance	Flux ($TeV^{-1}cm^{-2}s^{-1}$)
1	7.9	1.1 ± 0.2 E-14
2	8.4	1.3 ± 0.2 E-14
3	9.3	1.4 ± 0.2 E-14

Table 3.10: he significance and flux for 2HWC J1928+177 at the updated location modeled as a point source in 3 separate epochs each with an observation period of ∼508 days.

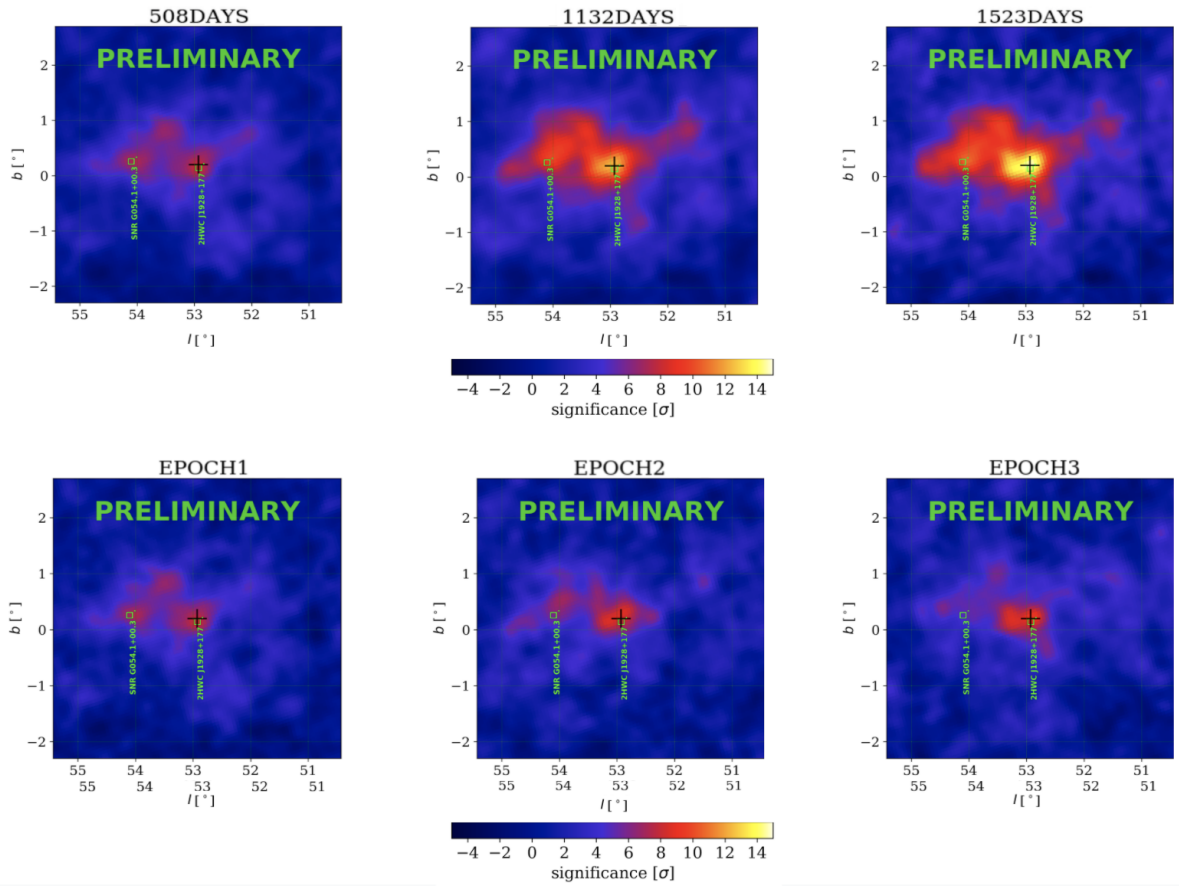

Figure 3.6: Three point source maps of cumulative HAWC data for 2HWC J1928+177 for 508 days of data (top left), 1132 days of data (top center), and 1523 days of data (top right). Three point source maps of HAWC data of 2HWC J1928+177 in Epoch 1 (bottom left), Epoch 2 (bottom center), and Epoch 3 (bottom right). The vertical axes show galactic latitude in degrees, while the horizontal axes show galactic longitude in degrees. The color scale indicates the significance of the source. The square is the source location based on the 2HWC catalog, the cross is the updated location.

3HWC J1928+178 resides in a very complex region, which presents many challenges for our morphological investigations. The 5 degree radius surrounding 3HWC J1928+178 contains three identified pulsars- PSR J1928+1746, PSR J1930+1852, and PSR J1932+1916. When we model

3HWC J1928+178 as an 0.5° extended source, there is some source confusion. On the other hand, VERITAS has set very tight constraints (at the level of 1% of the Crab Nebula) on a point source at this location (see Figure 3.7) [37]. However, VERITAS has a lower energy range than HAWC and does not have the same sensitivity to extended sources. Therefore, 3HWC J1928+178 must be an extended source because we observe a consistent excess. While 3HWC J1928+178 is also not detected by Fermi-LAT, the unassocited Fermi source 4FGL J1928.4+1801c is 0.2° away [38]. We believe these sources have a possible association to each other. This region is currently being studied in more detail by the HAWC Collaboration [39].

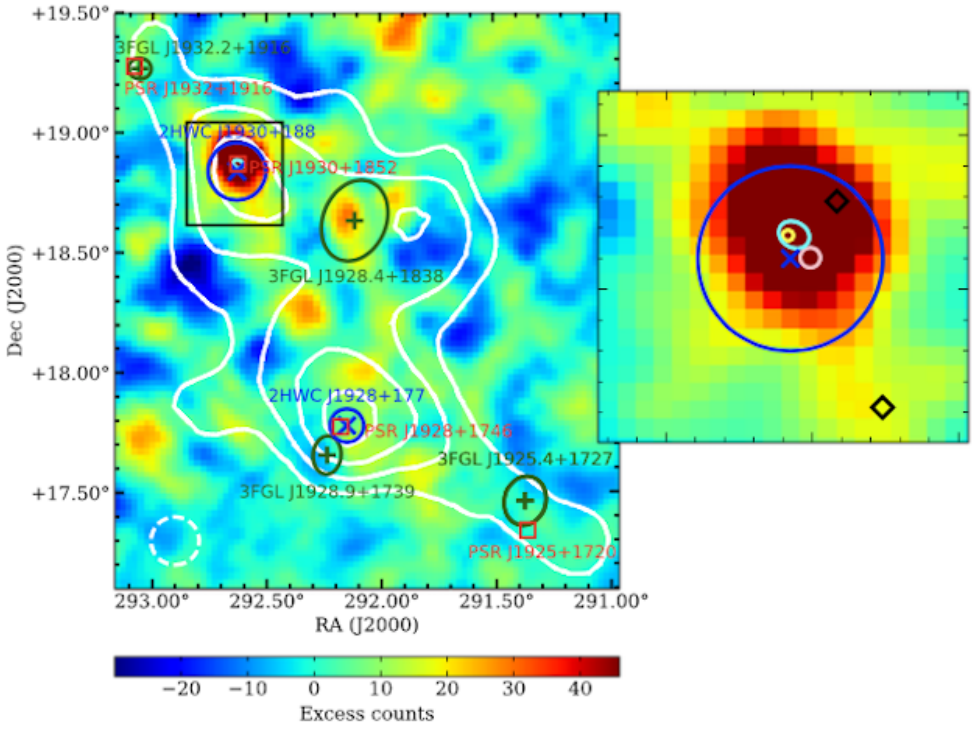

Figure 3.7: VERITAS map for the SNR G54.1+0.3 region. The location of 2HWC J1928+177 can be seen towards the bottom of the plot, though no corresponding gamma-ray excess is present [37]. The color scale indicates the gamma-ray excess counts in the VERITAS data. The white contors are from the 2HWC catalog. 2HWC sources are marked in blue, pulsars are marked in red, and 3FGL sources are marked in green.

3.1.6 2HWC J1938+238

2HWC J1938+238 was classified as a point source in the 2HWC catalog [4]. We update the location of maximum significance from $l = 59.37^\circ$, $b = 0.94^\circ$ [4] to $l = 59.47^\circ$, $b = 0.68^\circ$. The updated location is 0.28° from the original location, which is larger than the location uncertainty of 0.13° reported in the 2HWC catalog [4]. Examining the temporal progression of this excess at the updated location of maximum significance, we conclude that 2HWC J1938+238 remains a candidate TeV source. This excess is present in the 3HWC catalog as the point source 3HWC J1940+237 [5].

At its updated location, we find that 2HWC J1938+238 is located approximately 0.17° away from the middle-aged radio pulsar PSR J1940+2337 [4, 40, 41]. Although 2HWC J1938+238 surpassed the significance threshold in the 2HWC blind point source search [4], our temporal studies indicate that this detection is better modeled as a slightly extended source with a possible association to PSR J1940+2337. In addition, VERITAS performed an investigation of 2HWC J1938+238 at the original location designated by the 2HWC blind point source search. In VERITAS's investigation of this excess with a point source assumption, they find that the upper limits of the flux are lower than expected by more than one standard deviation from HAWC's data [37]. Our analysis supports the hypothesis that this is an extended source. A preliminary more detailed analysis of this region is presented in the Appendix.

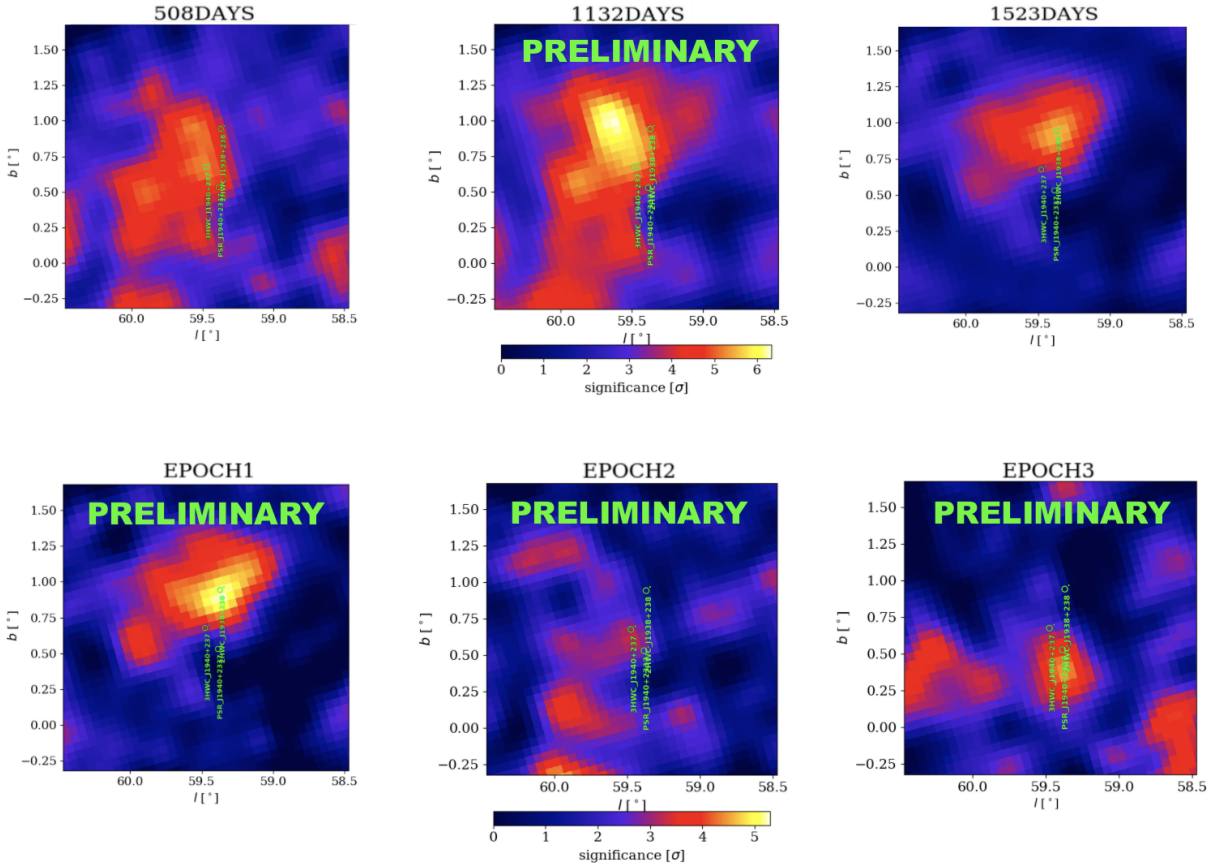

Figure 3.8: Three point source maps of cumulative HAWC data for 2HWC J1938+238 for 508 days of data (top left), 1132 days of data (top center), and 1523 days of data (top right). Three point source maps of HAWC data of 2HWC J1938+238 in Epoch 1 (bottom left), Epoch 2 (bottom center), and Epoch 3 (bottom right). The vertical axes show galactic latitude in degrees, while the horizontal axes show galactic longitude in degrees. The color scale indicates the significance of the source.

Observation Period	Actual Significance	Expected Significance	Percent Error
508 Days	3.6	-	-
1132 Days	5.4	5.4	0.3
1523 Days	5.2	6.3	17.0

Table 3.11: The significance progression for 2HWC J1938+238 at the new location modeled as a point source for three cumulative observation periods.

Epoch	Significance	Flux ($\text{TeV}^{-1}\text{cm}^{-2}\text{s}^{-1}$)
1	3.1	$5 \pm$ 2E-15
2	3.2	$4 \pm$ 1E-15
3	2.7	$4 \pm$ 2E-15

Table 3.12: The significance and flux for 2HWC J1938+238 modeled as a point source in 3 separate epochs each with an observation period of ∼508 days.

3.1.7 2HWC J1949+244

2HWC J1949+244 was classified as a 1.0° extended source in the 2HWC catalog [4]. We update the location of maximum significance from $l = 61.16^\circ$, $b = -0.85^\circ$ [4] to $l = 60.90^\circ$, $b = -0.58^\circ$. The updated location is 0.37° from the original location, which falls into the location uncertainty of 0.71° reported in the 2HWC catalog [4]. Examining the temporal progression of this excess at the updated location, we conclude that 2HWC J1949+244 remains a candidate TeV source. Because this excess now passes the significance threshold with a point source model, it is present in the 3HWC catalog as the point source 3HWC J1950+242 [5].

Although 2HWC J1949+244 surpassed the significance threshold in the 3HWC blind point source search [5], our temporal studies indicate that this detection is better modeled as a slightly extended source. With a point source model, we find that the location of maximum significance for 2HWC J1949+244 is $l = 61.10^\circ$, $b = -1.16^\circ$, in agreement with the 3HWC catalog [5]. In addition, we find that this new location is 0.45° from the unassociated Fermi-LAT source 3FGL J1949.3+2433 and nearly coincident with the binary pulsar PSR J1950+2414 [42, 43]. A preliminary more detailed analysis of this region is presented in the Appendix.

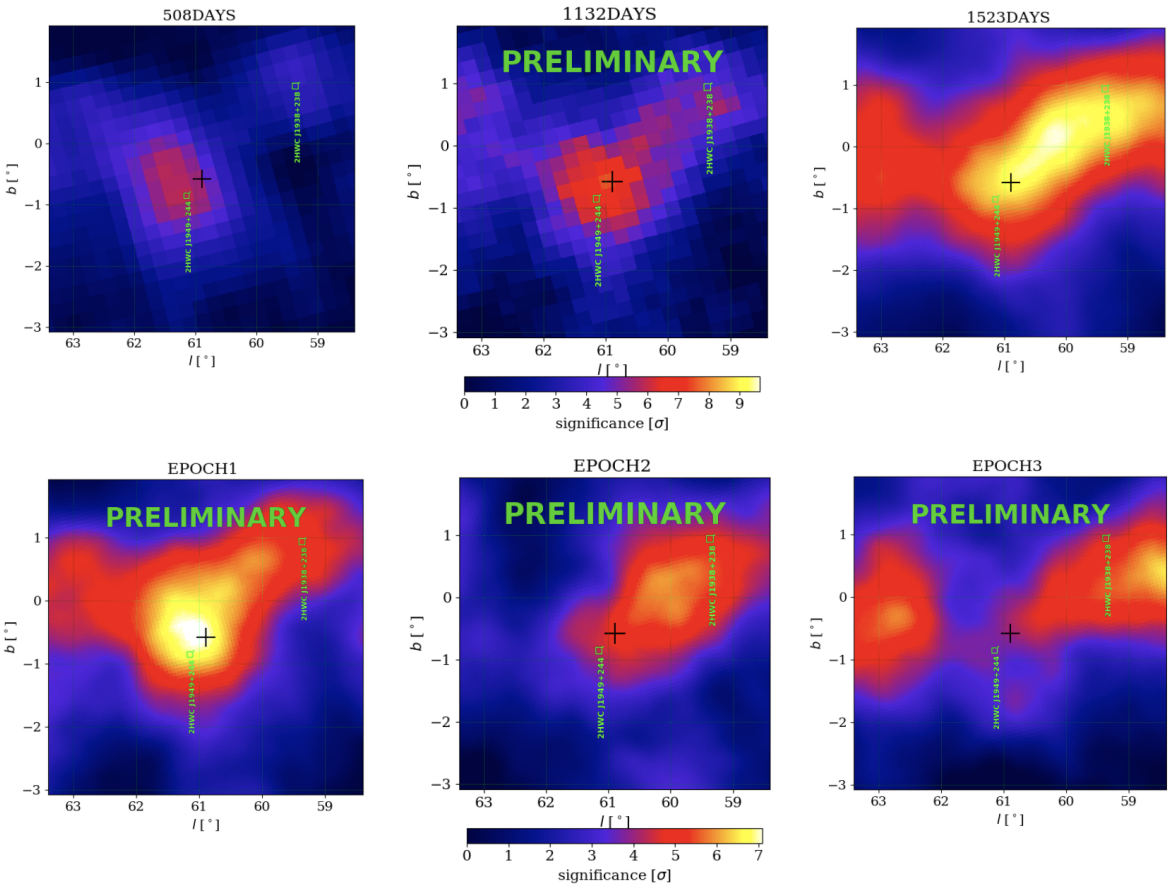

Figure 3.9: Three 1.0° extended source maps of cumulative HAWC data for 2HWC J1949+244 for 508 days of data (top left), 1132 days of data (top center), and 1523 days of data (top right). Three 1.0° extended source maps of HAWC data of 2HWC J1953+294 in Epoch 1 (bottom left), Epoch 2 (bottom center), and Epoch 3 (bottom right). The vertical axes show galactic latitude in degrees, while the horizontal axes show galactic longitude in degrees. The color scale indicates the significance of the source. The square is the source location based on the 2HWC catalog, the cross is the updated location.

Observation Period	Actual Significance	Expected Significance	Percent Error
508 Days	5.5	-	-
1132 Days	7.5	8.2	9.1
1523 Days	9.3	8.7	6.7

Table 3.13: The significance progression for 2HWC J1949+244 at the new location modeled as a 1.0° extended source for three cumulative observation periods.

Epoch	Significance	Flux ($\text{TeV}^{-1}\text{cm}^{-2}\text{s}^{-1}$)
1	7.0	3.5 ± 0.5 E-12
2	4.5	2.3 ± 0.5 E-12
3	3.8	2.0 ± 0.5 E-12

Table 3.14: The significance and flux for 2HWC J1949+244 at the updated location modeled as a 1.0° extended source in 3 separate epochs each with an observation period of $\sim$508 days.

3.1.8 2HWC J1953+294

2HWC J1953+294 was classified as a point source in the 2HWC catalog [4]. We update the location of maximum significance from $l = 65.86^\circ$, $b = 1.07^\circ$ [4] to $l = 65.66^\circ$, $b = 1.23^\circ$. The updated location is 0.26° from the original location, which is comperable to the location uncertainty of 0.24° reported in the 2HWC catalog [4]. Examining the temporal progression of this excess at the updated location of maximum significance, we conclude that 2HWC J1953+294 remains a candidate TeV source. This excess is present in the 3HWC catalog as the point source 3HWC J1951+293 [5].

Observation Period	Actual Significance	Expected Significance	Percent Error
508 Days	5.2	-	-
1132 Days	7.6	7.8	2.9
1523 Days	8.3	8.8	5.3

Table 3.15: The significance progression for 2HWC J1953+294 at the updated location modeled as a point source for three cumulative observation periods.

Epoch	Significance	Flux ($\text{TeV}^{-1}\text{cm}^{-2}\text{s}^{-1}$)
1	4.8	1.1 ± 0.2 E-12
2	5.7	1.2 ± 0.2 E-12
3	3.9	9 ± 2 E-13

Table 3.16: The significance and flux for 2HWC J1953+294 at the updated location modeled as a point source in 3 separate epochs each with an observation period of $\sim$508 days.

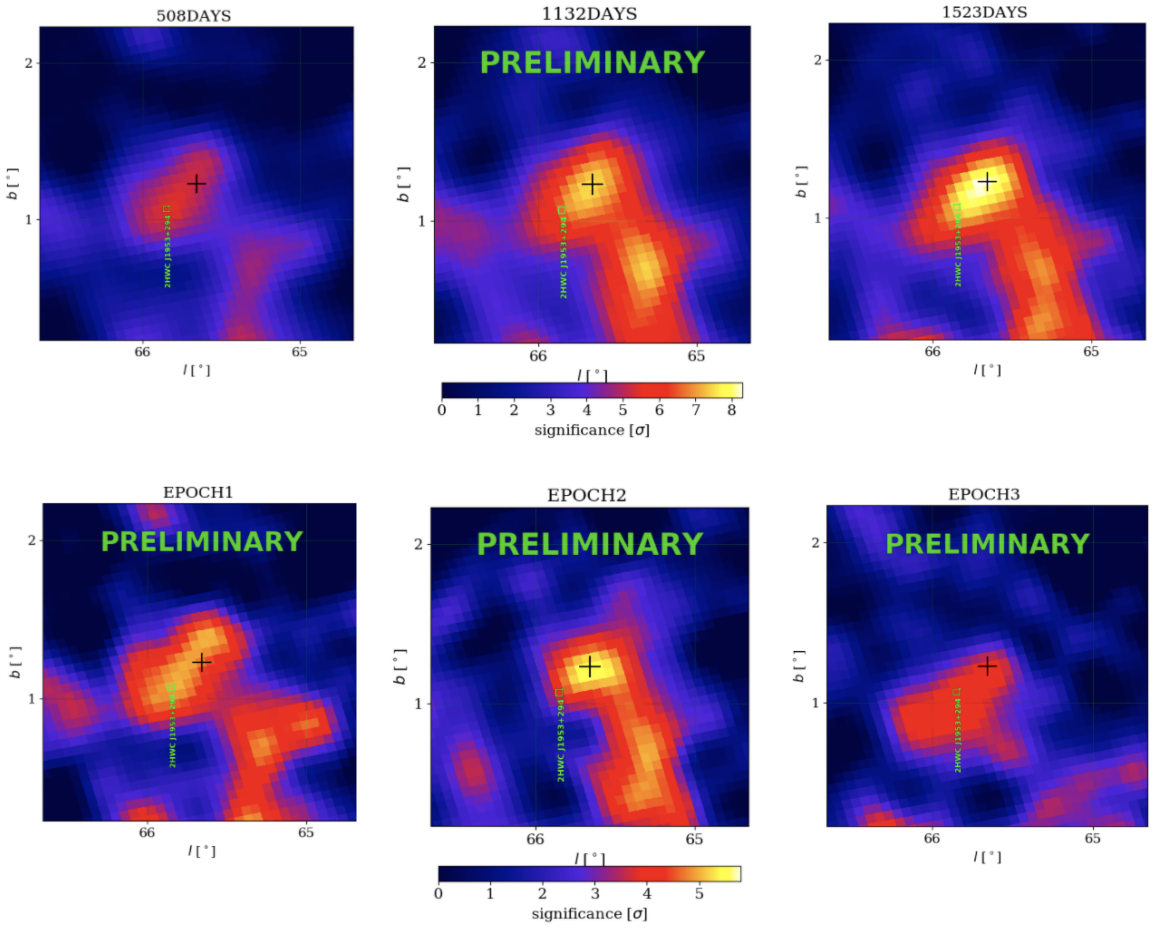

Figure 3.10: Three point source maps of cumulative HAWC data for 2HWC J1953+294 for 508 days of data (top left), 1132 days of data (top center), and 1523 days of data (top right). Three point source maps of HAWC data of 2HWC J1953+294 in Epoch 1 (bottom left), Epoch 2 (bottom center), and Epoch 3 (bottom right). The vertical axes show galactic latitude in degrees, while the horizontal axes show galactic longitude in degrees. The color scale indicates the significance of the source. The square is the source location based on the 2HWC catalog, the cross is the updated location.

3.1.9 2HWC J1955+285

2HWC J1955+285 was classified as a point source in the 2HWC catalog [4]. We update the location of maximum significance from $l = 65.35°$, $b = 0.18°$ [4] to $l = 65.32°$, $b = 0.30°$. The updated location is $0.12°$ from the original location, which falls into the location uncertainty of $0.14°$ reported in the 2HWC catalog [4]. Examining the temporal progression of this excess at the updated location of maximum significance, we conclude that 2HWC J1955+285 remains a candidate TeV source. However, 2HWC J1955+285 only passes the secondary source TS criteria because it is not separated from nearby sources with a large TS gap. This excess is present in the 3HWC catalog as the point source 3HWC J1954+286† [5].

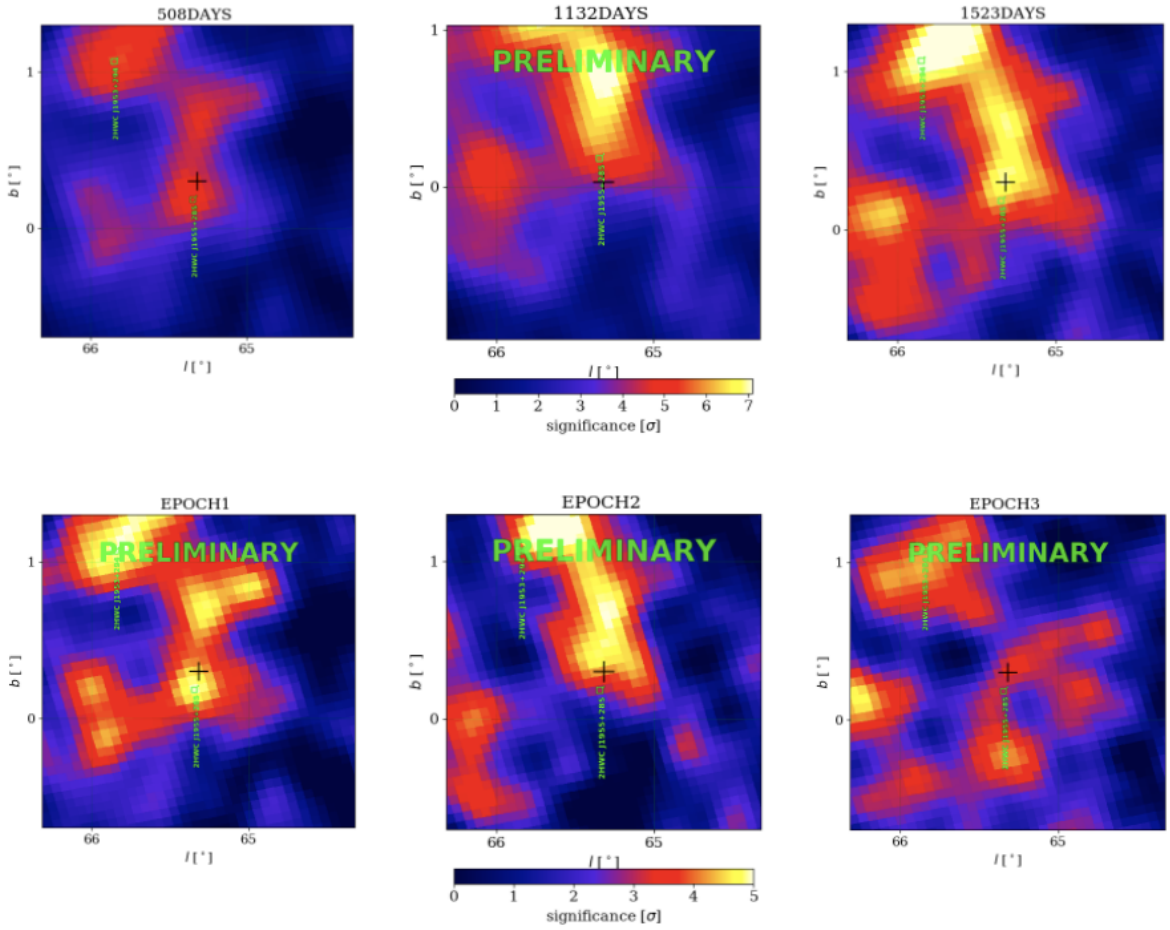

Figure 3.11: Three point source maps of cumulative HAWC data for 2HWC J1955+285 for 508 days of data (top left), 1132 days of data (top center), and 1523 days of data (top right). Three point source maps of HAWC data of 2HWC J1955+285 in Epoch 1 (bottom left), Epoch 2 (bottom center), and Epoch 3 (bottom right). The vertical axes show galactic latitude in degrees, while the horizontal axes show galactic longitude in degrees. The color scale indicates the significance of the source. The square is the source location based on the 2HWC catalog, the cross is the updated location.

Observation Period	Actual Significance	Expected Significance	Percent Error
508 Days	4.7	-	-
1132 Days	6.2	7.1	11.8
1523 Days	7.0	7.2	3.9

Table 3.17: The significance progression for 2HWC J1955+285 at the updated location modeled as a point source for three cumulative observation periods.

Epoch	Significance	Flux ($\text{TeV}^{-1}\text{cm}^{-2}\text{s}^{-1}$)
1	4.9	10 ± 2 E-13
2	4.4	10 ± 2 E-13
3	3.4	7 ± 2 E-13

Table 3.18: The significance and flux for 2HWC J1955+285 at the updated location modeled as a point source in 3 separate epochs each with an observation period of $\sim$508 days.

3.1.10 2HWC J2006+341

2HWC J2006+341 was classified as a point source in the 2HWC catalog [4]. We update the location of maximum significance from $l = 71.33°$, $b = 1.16°$ [4] to $l = 71.25°$, $b = 0.94°$. The updated location is $0.23°$ from the original location, which is larger than the location uncertainty of $0.13°$ reported in the 2HWC catalog [4]. Examining the temporal progression of this excess at the updated location of maximum significance, we conclude that 2HWC J2006+341 remains a candidate TeV source. This excess is present in the 3HWC catalog as the point source 3HWC J2006+340 [5]. Although 2HWC J2006+341 surpassed the significance threshold in the 2HWC blind point source search [4], our temporal studies indicate that this detection is better modeled with an extension between 0.5° and 1.0°. Since its original discovery 2HWC J2006+341, has been studied in greater detail by both HAWC and Fermi-LAT and is better fitted with an extension of 0.9° when modeled as a disk and 0.7° when modeled as a Gaussian [44].

Observation Period	Actual Significance	Expected Significance	Percent Error
508 Days	5.08	-	-
1132 Days	6.94	7.6	8.5
1523 Days	8.21	8.1	2.0

Table 3.19: The significance progression for 2HWC J2006+341 at the updated location modeled as a point source for three cumulative observation periods.

Epoch	Significance	Flux ($\text{TeV}^{-1}\text{cm}^{-2}\text{s}^{-1}$)
1	5.0	1.1 ± 0.2 E-12
2	4.3	10 ± 2 E-13
3	5.8	1.3 ± 0.2 E-12

Table 3.20: The significance and flux for 2HWC J2006+341 at the updated location modeled as a point source in 3 separate epochs each with an observation period of $\sim$508 days.

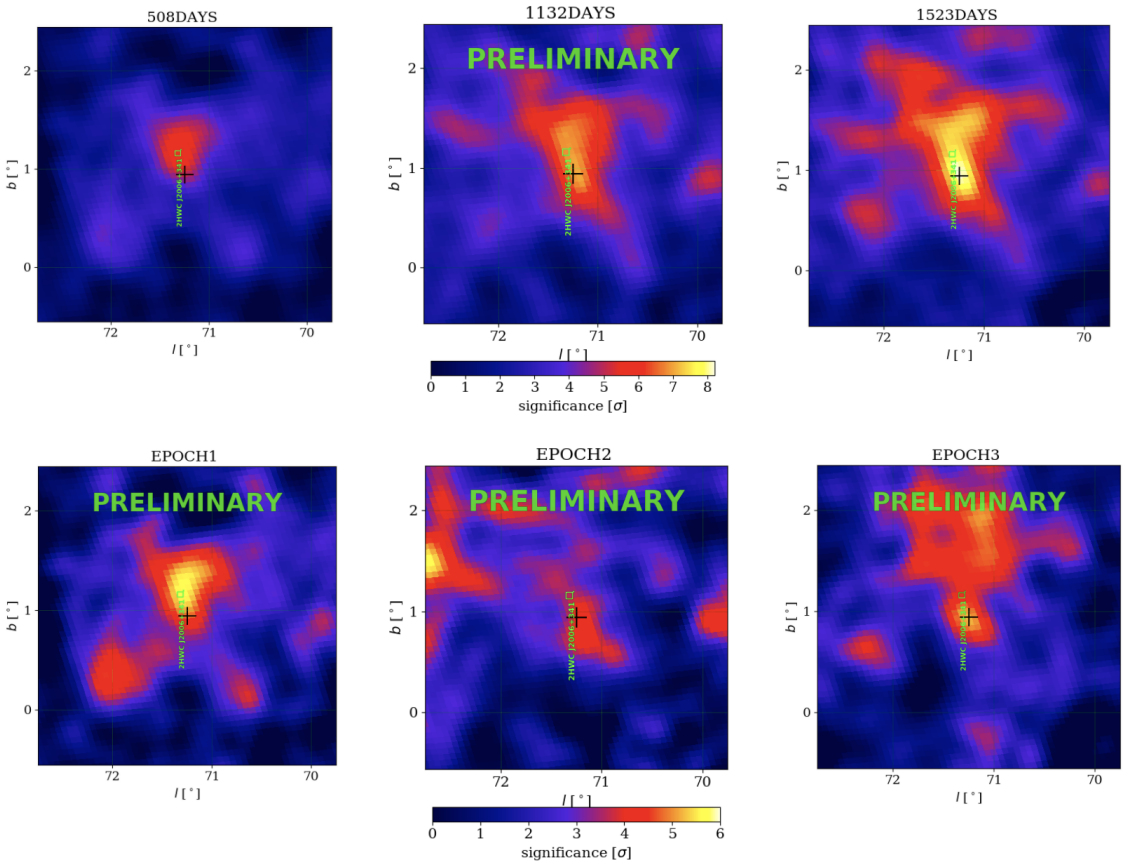

Figure 3.12: Three point source maps of cumulative HAWC data for 2HWC J2006+341 for 508 days of data (top left), 1132 days of data (top center), and 1523 days of data (top right). Three point source maps of HAWC data of 2HWC J2006+341 in Epoch 1 (bottom left), Epoch 2 (bottom center), and Epoch 3 (bottom right). The vertical axes show galactic latitude in degrees, while the horizontal axes show galactic longitude in degrees. The color scale indicates the significance of the source. The square is the source location based on the 2HWC catalog, the cross is the updated location.

3.2 Other Candidates

In this section, we will discuss the excesses that are no longer classified as a candidate TeV source. For this reason, we present a representative sample in Figure 3.13 of an excess that is no longer considered a candidate TeV source.

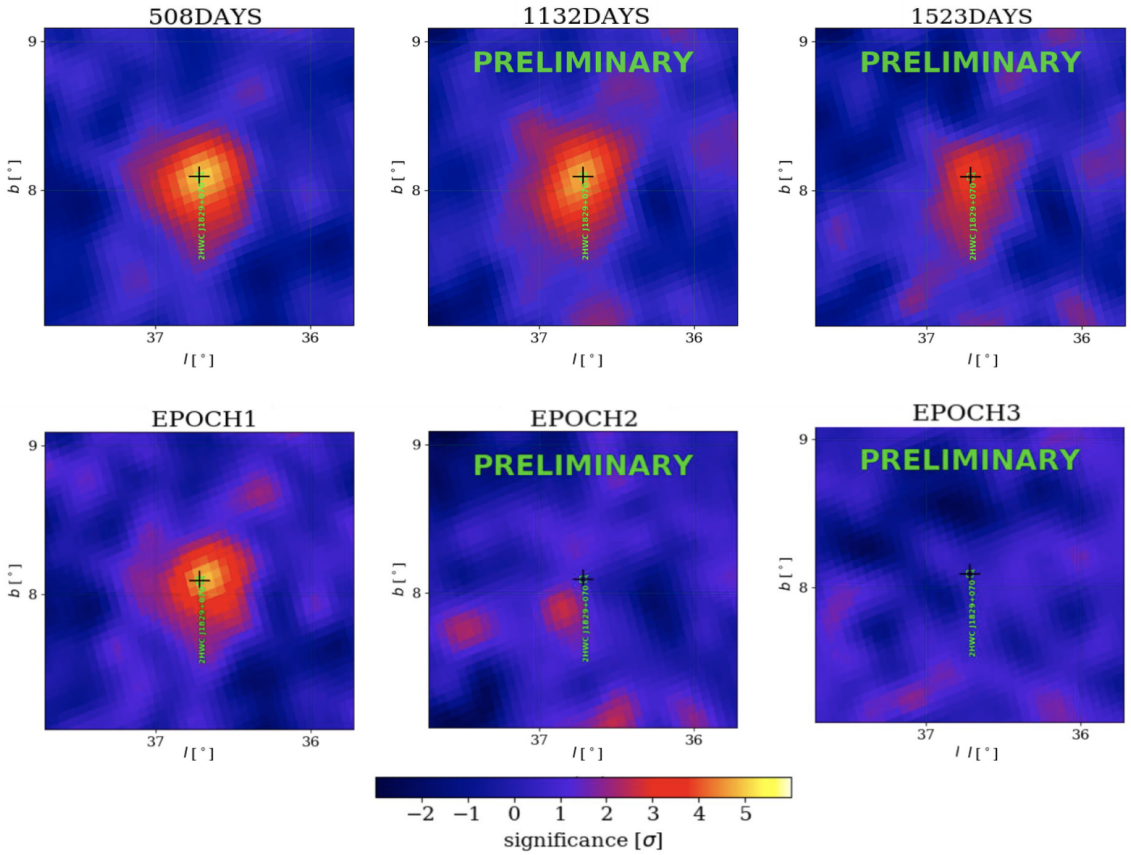

Figure 3.13: Three point source maps of cumulative HAWC data for 2HWC J1829+070 with 508 days of data (top left), 1132 days of data (top center), and 1523 days of data (top right). Three point source maps of HAWC data of 2HWC J1829+070 in Epoch 1 (bottom left), Epoch 2 (bottom center), and Epoch 3 (bottom right). The vertical axes show galactic latitude in degrees, while the horizontal axes show galactic longitude in degrees. The color scale indicates the significance of the source.

3.2.1 2HWC J0819+157

2HWC J0819+157 was classified as a $0.5°$ extended source in the 2HWC catalog [4]. The location of maximum significance remains $l = 208.00°$, $b = 26.52°$, in agreement with the 2HWC catalog [4]. Examining the temporal progression of this excess at the location of maximum significance, we conclude that 2HWC J0819+157 is no longer classified as a candidate TeV source. This excess is not be present in the 3HWC catalog [5].

3.2.2 2HWC J1040+308

2HWC J1040+308 was classified as a $0.5°$ extended source in the 2HWC catalog [4]. The location of maximum significance remains $l = 197.59°$, $b = 61.31°$, in agreement with the 2HWC catalog [4]. Examining the temporal progression of this excess at the location of maximum significance, we conclude that 2HWC J1040+308 is no longer classified as a candidate TeV source. This

Observation Period	Actual Significance	Expected Significance	Percent Error
508 Days	5.5	-	-
1132 Days	4.8	8.3	42.6
1523 Days	4.0	5.5	27.4

Table 3.21: The significance progression for 2HWC J0819+157 modeled as a 0.5° extended source for three cumulative observation periods.

Epoch	Significance	Flux ($\text{TeV}^{-1}\text{cm}^{-2}\text{s}^{-1}$)
1	4.7	1.5 ± 0.3 E-12
2	2.0	7 ± 3 E-13
3	0.5	2 ± 2 E-13

Table 3.22: The significance and flux for 2HWC J0819+157 modeled as a 0.5° extended source in 3 separate epochs each with an observation period of $\sim$508 days.

excess is not be present in the 3HWC catalog [5]. In an earlier work, Coronado-Blázquez, 2019 [45] hypothesised that 2HWC J1040+308 is a product of the self-annihilation of weakly interacting massive particles (WIMPs) in the Milky Way's dark matter subhalos, though with this new data it is unlikely that this is the case.

Observation Period	Actual Significance	Expected Significance	Percent Error
508 Days	5.3	-	-
1132 Days	4.2	7.9	46.6
1523 Days	2.7	4.9	44.4

Table 3.23: The significance progression for 2HWC J1040+308 modeled as a 0.5° extended source for three cumulative observation periods.

Epoch	Significance	Flux ($\text{TeV}^{-1}\text{cm}^{-2}\text{s}^{-1}$)
1	5.4	1.8 ± 0.4 E-12
2	1.4	5 ± 4 E-13
3	0	0

Table 3.24: The significance and flux for 2HWC J1040+308 modeled as a 0.5° extended source in 3 separate epochs each with an observation period of $\sim$508 days.

3.2.3 2HWC J1309-054

2HWC J1309-054 was classified as a point source in the 2HWC catalog [4]. The location of maximum significance remains $l = 311.11°$, $b = 57.10°$, in agreement with the 2HWC catalog [4]. Examining the temporal progression of this excess at the location of maximum significance, we conclude that 2HWC J1309-054 is no longer classified as a candidate TeV source. This excess is not be present in the 3HWC catalog [5].

Observation Period	Actual Significance	Expected Significance	Percent Error
508 Days	5.0	-	-
1132 Days	1.8	7.5	76.6
1523 Days	1.5	2.0	25.5

Table 3.25: The significance progression for 2HWC J1309-054 modeled as a point source for three cumulative observation periods.

Epoch	Significance	Flux ($TeV^{-1}cm^{-2}s^{-1}$)
1	4.6	1.5 ± 0.4 E-12
2	0	0
3	0	0

Table 3.26: The significance and flux for 2HWC J1309-054 modeled as a point source in 3 separate epochs each with an observation period of $\sim$508 days.

3.2.4 2HWC J1829+070

2HWC J1829+070 was classified as a point source in the 2HWC catalog [4]. The location of maximum significance remains $l = 36.72°$, $b = 8.09°$, in agreement with the 2HWC catalog [4]. Examining the temporal progression of this excess at the location of maximum significance, we conclude that 2HWC J1829+070 is no longer classified as a candidate TeV source. This excess is not be present in the 3HWC catalog [5].

Observation Period	Actual Significance	Expected Significance	Percent Error
508 Days	5.0	-	-
1132 Days	4.7	7.5	36.9
1523 Days	3.6	5.5	35.4

Table 3.27: The significance progression for 2HWC J1829+070 modeled as a point source for three cumulative observation periods.

Epoch	Significance	Flux ($\text{TeV}^{-1}\text{cm}^{-2}\text{s}^{-1}$)
1	4.8	1.1 ± 0.2 E-12
2	0.8	1.8 ± 0.2 E-12
3	0.5	1.2 ± 0.2 E-12

Table 3.28: The significance and flux for 2HWC J1829+070 modeled as a point source in 3 separate epochs each with an observation period of ∼508 days.

3.2.5 2HWC J1902+048*

2HWC J1902+048* was classified as a point source in the 2HWC catalog [4]. We update the location of maximum significance from $l = 38.46°, b = -0.14°$ [4] to $l = 38.52°, b = -0.11°$. The updated location is $0.26°$ from the original location, which is greater than the location uncertainty of $0.18°$ reported in the 2HWC catalog [4]. Examining the temporal progression of this excess at the updated location of maximum significance, we find that 2HWC J1902+048* does not pass the TS valley gap. For this reason, 2HWC J1902+048* is no longer classified as a candidate TeV source. That being said, this excess is now considered part of the complex region surrounding the Milagro source MGRO J1908+06 [5]. MGRO J1908+06 is a known extended TeV source, which is associated with the pulsar wind nebula of the Fermi-LAT pulsar PSR J1907+0602 [46]. This excess is not be present in the 3HWC catalog [5].

Observation Period	Actual Significance	Expected Significance	Percent Error
508 Days	5.4	-	-
1132 Days	7.0	8.1	13.7
1523 Days	7.2	8.1	11.7

Table 3.29: The significance progression for 2HWC J1902+048* modeled as a point source for three cumulative observation periods.

Epoch	Significance	Flux ($\text{TeV}^{-1}\text{cm}^{-2}\text{s}^{-1}$)
1	5.7	1.5 ± 0.3 E-12
2	4.3	1.0 ± 0.3 E-12
3	4.5	1.1 ± 0.3 E-12

Table 3.30: The significance and flux for 2HWC J1902+048* modeled as a point source in 3 separate epochs each with an observation period of ∼508 days.

3.2.6 2HWC J1921+131

2HWC J1921+131 was classified as a point source in the 2HWC catalog [4]. We update the location of maximum significance from $l = 47.99°$, $b = -0.50°$ [4] to $l = 47.99°$, $b = -0.45°$.

The updated location is 0.05° from the original location, which falls into the location uncertainty of 0.12° reported in the 2HWC catalog [4]. Examining the temporal progression of this excess at the updated location of maximum significance, we conclude that 2HWC J1921+131 is no longer classified as a candidate TeV source. This excess is not be present in the 3HWC catalog [5].

Observation Period	Actual Significance	Expected Significance	Percent Error
508 Days	5.5	-	-
1132 Days	4.6	8.2	44.0
1523 Days	4.7	5.3	11.9

Table 3.31: The significance progression for 2HWC J1921+131 modeled as a point source for three cumulative observation periods.

Epoch	Significance	Flux ($\text{TeV}^{-1}\text{cm}^{-2}\text{s}^{-1}$)
1	5.4	1.1 ± 0.2 E-12
2	2.9	5.9 ± 0.2 E-12
3	2.4	2.8 ± 0.2 E-12

Table 3.32: The significance and flux for 2HWC J1921+131 modeled as a point source in 3 separate epochs each with an observation period of $\sim$508 days.

CHAPTER4

Conclusions and Future Work

In this work, we investigate the 16 candidate TeV sources detected in the blind surveys conducted by HAWC with a 508 day observation period [4]. Now, with 1523 cumulative days of observations, we update the locations of these excesses and reevaluate their extensions. We carry out temporal investigations of the statistical significance and flux for these excesses to determine if they have faded into the diffuse gamma radiation or if they can still be considered considered candidate TeV sources, and we compare our results to those presented in the newly released 3HWC catalog [5]. Further, we explore possible associations to detections from lower energy observatories. We conclude that 10 of the 16 excesses remain candidate TeV sources, while 6 of these excesses no longer qualify as candidate TeV sources.

In the future, we plan to explore the remaining candidate sources in more detail by carrying out robust analyses of their morphology and spectral energy distributions. (We present similar preliminary analyses for a selected subset of candidate sources in the Appendix). We also plan to apply statistical counterpart association techniques, such as Nway [47]. In addition, plan to perform similar investigations with the 20 new HAWC candidate sources with no TeV counterpart from the 3HWC catalog [5] and continually monitor new detections from observatories such as Fermi-LAT and VERITAS in order to discover any lower energy counterparts for these candidate sources. While many of these sources still do not have associations to detections from other observatories, they offer exciting potential for future study as we usher in new gamma-ray detectors such as the Cherenkov Telescope Array, which will form the largest and most sensitive high-energy gamma-ray telescope and revolutionize the field of ground-based gamma-ray astronomy [48]. As we begin to collect more data on these nascent candidate TeV sources, we hope to one day characterize their spectral energy distributions for a large range of energies. More complete spectral energy distributions will allow us to characterize the gamma-ray production mechanisms present in these sources. With this information, we will be able to better understand the acceleration mechanisms present in extreme astrophysical phenomena such as supernova remnants, gamma-ray bursts, and pulsars.

Appendix

5.1 2D Binning Scheme

We use the fraction hit or *fhit* bins to describe the size of a shower (Table 4.1). We define the shower size as the ratio of PMTs hit within the first 20 nanoseconds of the shower to the number of channels available during the event. We use the energy bins to describe the energy range of a shower (Table 4.2). When fitting the spectrum of a source, it is necessary to consider both the size and energy of a shower because the angular resolution of HAWC varies based on these two factors [35]. For this reason, we fit our spectral energy distributions using a 2D binning scheme that takes into account both shower size and energy. Additionally, the energy of a shower is heavily dependent on its zenith angle. Therefore, we take into account the differences in energy distribution caused by differences in source declination by using only specific 2D bins for a source of given declination (Table 4.3) [35, 22, 36].

Bin	fHit Range
1	6.7 - 10.5
2	10.5 - 16.2
3	16.2 - 24.7
4	24.7 - 35.6
5	35.6 - 48.5
6	48.5 - 61.8
7	61.8 - 74.0
8	74.0 - 84.0
9	84.0 - 1.00

Table 4.1: fHit Bin Designations [35]

Bin	Energy Range (TeV)
a	0.316 - 0.562
b	0.562 - 1.0
c	1.0 - 1.78
d	1.78 - 3.16
e	3.16 - 5.62
f	5.62 - 10.0
g	10.0 - 17.8
h	17.8 - 31.6
i	31.6 - 56.2
j	56.2 - 100
k	100 - 177
l	177 - 316

Table 4.2: Energy Bin Designations [35]

Declination	Corresponding 2D Bins
-25	1d 1e 1f 2d 2e 2f 3e 3f 3g 4f 4g 4h 5f 5g 5h 6g 6h 6i 7i 8j 9i 9j 9k 9l
-20	1d 1e 1f 1g 2d 2e 2f 3e 3f 3g 4e 4f 4g 4h 5f 5g 5h 6g 6h 6i 7h 7i 8i 8j 9i 9j 9k 9l
-15	1c 1d 1e 1f 2c 2d 2e 2f 3d 3e 3f 3g 4d 4e 4f 4g 4h 5f 5g 5h 6f 6g 6h 6i 7g 7h 7i 8h 8i 8j 9h 9i 9j 9k 9l
-10	1c 1d 1e 1f 2c 2d 2e 2f 3c 3d 3e 3f 4d 4e 4f 4g 5e 5f 5g 5h 6f 6g 6h 6i 7g 7h 7i 8g 8h 8i 8j 9h 9i 9j 9k 9l
-5	1c 1d 1e 1f 2c 2d 2e 2f 3c 3d 3e 3f 4d 4e 4f 4g 5d 5e 5f 5g 5h 6e 6f 6g 6h 6i 7f 7g 7h 7i 8g 8h 8i 8j 9h 9i 9j 9k 9l
0	1c 1d 1e 1f 2c 2d 2e 2f 3c 3d 3e 3f 3g 4d 4e 4f 4g 5d 5e 5f 5g 5h 6e 6f 6g 6h 7f 7g 7h 7i 8g 8h 8i 8j 9g 9h 9i 9j 9k 9l
5	1c 1d 1e 2c 2d 2e 2f 3c 3d 3e 3f 4c 4d 4e 4f 4g 5d 5e 5f 5g 5h 6e 6f 6g 6h 7f 7g 7h 7i 8g 8h 8i 8j 9g 9h 9i 9j 9k 9l
10	1c 1d 1e 2c 2d 2e 3c 3d 3e 3f 4c 4d 4e 4f 4g 5d 5e 5f 5g 5h 6e 6f 6g 6h 7f 7g 7h 7i 8f 8g 8h 8i 8j 9g 9h 9i 9j 9k 9l
15	1c 1d 1e 2c 2d 2e 3c 3d 3e 3f 4c 4d 4e 4f 4g 5d 5e 5f 5g 5h 6d 6e 6f 6g 6h 7f 7g 7h 7i 8f 8g 8h 8i 8j 9g 9h 9i 9j 9k 9l
20	1c 1d 1e 2c 2d 2e 3c 3d 3e 3f 4c 4d 4e 4f 4g 5d 5e 5f 5g 5h 6d 6e 6f 6g 6h 7f 7g 7h 7i 8f 8g 8h 8i 8j 9g 9h 9i 9j 9k 9l
25	1c 1d 1e 2c 2d 2e 3c 3d 3e 3f 4c 4d 4e 4f 4g 5d 5e 5f 5g 5h 6e 6f 6g 6h 7f 7g 7h 7i 8f 8g 8h 8i 8j 9g 9h 9i 9j 9k 9l
30	1c 1d 1e 2c 2d 2e 3c 3d 3e 3f 4c 4d 4e 4f 4g 5d 5e 5f 5g 5h 6e 6f 6g 6h 7f 7g 7h 7i 8f 8g 8h 8i 8j 9g 9h 9i 9j 9k 9l
35	1c 1d 1e 2c 2d 2e 2f 3c 3d 3e 3f 4c 4d 4e 4f 4g 5d 5e 5f 5g 5h 6e 6f 6g 6h 7f 7g 7h 7i 8g 8h 8i 8j 9g 9h 9i 9j 9k 9l
40	1c 1d 1e 1f 2c 2d 2e 2f 3c 3d 3e 3f 4c 4d 4e 4f 4g 5e 5f 5g 5h 6e 6f 6g 6h 7f 7g 7h 7i 8g 8h 8i 8j 9g 9h 9i 9j 9k 9l
45	1c 1d 1e 1f 2c 2d 2e 2f 3c 3d 3e 3f 4d 4e 4f 4g 5e 5f 5g 5h 6e 6f 6g 6h 6i 7g 7h 7i 8g 8h 8i 8j 9h 9i 9j 9k 9l
50	1c 1d 1e 1f 2c 2d 2e 2f 3d 3e 3f 3g 4d 4e 4f 4g 5e 5f 5g 5h 6f 6g 6h 6i 7g 7h 7i 8h 8i 8j 9h 9i 9j 9k 9l
55	1c 1d 1e 1f 2d 2e 2f 3d 3e 3f 3g 4e 4f 4g 4h 5e 5f 5g 5h 6f 6g 6h 6i 7g 7h 7i 8h 8i 8j 9i 9j 9k 9l
60	1d 1e 1f 1g 2d 2e 2f 3e 3f 3g 4e 4f 4g 4h 5f 5g 5h 6g 6h 6i 7h 7i 7j 8i 8j 9i 9j 9k 9l

Table 4.3: Ground Parameter 2D Binning Scheme for Given Declination [36]

5.2 Preliminary Detailed Analysis of the Region Containing 2HWC J1949+244 and 2HWC J1938+238

In this section, we discuss preliminary model hypotheses for the region containing 2HWC J1949+244 and 2HWC J1938+238 and preliminary spectral energy distributions. We decide to perform our morphological fits with the 1523 day dataset, which is constructed with a 1D binning scheme ased on shower size. However, for our spectral fits we find that it is best to use a 2D binning scheme (see Section 2.4). Due to the nature of HAWC's extensive air shower reconstruction methods and the fact that the detector was still under construction for the first ∼200 days of observations, we make cuts to the dataset used for spectral fits in order to increase our confidence in proper energy measurements. The cut dataset we use for our spectral fits comprises 1343 days of observations.

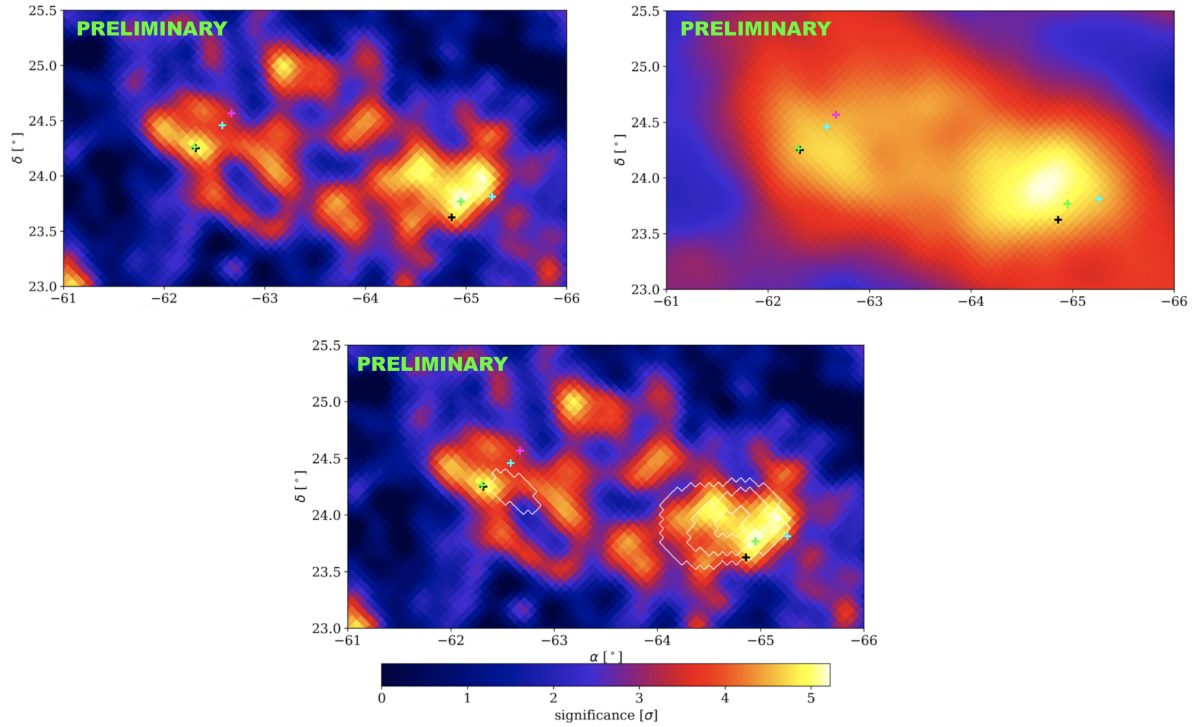

Figure 4.1: Maps of HAWC data for 2HWC J1949+244 and 2HWC J1938+238. At the top left we present a point source map, at the top right we present a $0.5°$ extended map, and at the bottom a point source map a contor overlay from the $0.5°$ extended map. The vertical axes show declination δ in degrees, while the horizontal axes show right ascension α in degrees. The color scale indicates the significance of the source. In the 2HWC J1949+244 region (left): the black cross marks the location of PSR J1950+2414, the green cross marks the location of 3HWC J1950+242, the cyan cross marks the location of 2HWC J1949+244, and the pink cross marks the location of 3FGL J1949.3+2433 [49, 5, 4]. In the 2HWC J1938+238 region (right): the black cross marks the location of PSR J1940+2337, the green cross marks the location of 3HWC J1940+237, and the cyan cross marks the location of 2HWC J1938+238 [49, 5, 4].

We present the significance maps of the region containing 2HWC J1949+244 and 2HWC J1938+238 (see Figure 4.1). We will refer to the significant region on the left as the 2HWC J1949+244 region and the significant region on the right as the 2HWC J1938+238 region. Note that these maps are presented in equatorial coordinates so that it is easier to see the region containing both sources.

5.2.1 2HWC J1949+244

First, we model the morphology of the 2HWC J1949+244 region using 3ML and the HAL plugin [34]. We use a region of interest of 1°. We assume a simple power law spectrum with a pivot energy of 7 TeV and a Gaussian shape. We fit the extension of this region with a location coincident with the point of maximum significance in the point source map, which is also coincident with the location of PSR J1950+2414 ($\alpha = 297.69^\circ$, $\delta = 24.26^\circ$) [49, 5]. We find that the extension is best fit to $0.6 \pm 0.1^\circ$. We present maps of the region, source model, and residuals in Figure 4.2.

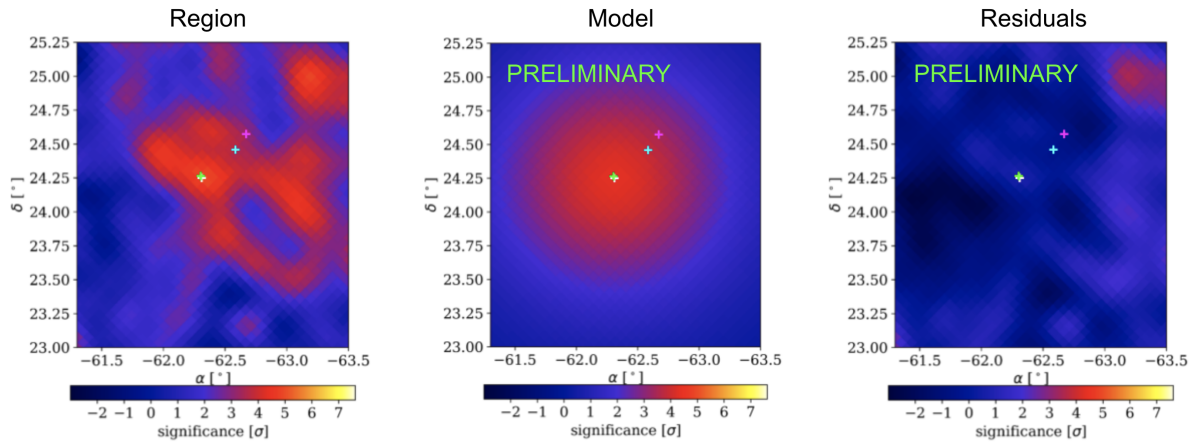

Figure 4.2: 3 maps of HAWC data for 2HWC J1949+244. The left map presents the region containing the source, the middle map presents the model for the source, and the right map presents the residuals. The white cross marks the location of PSR J1950+2414, the green cross marks the location of 3HWC J1950+242, the cyan cross marks the location of 2HWC J1949+244, and the pink cross marks the location of 3FGL J1949.3+2433 [49, 5, 4].

We expect the histogram of the residuals for this region to follow a Gaussian distribution with a mean of 0 and width of 1. We find that our data have a mean of 0.070 ± 0.034 and a width of 0.952 ± 0.033, which indicate that our model is a good fit (see Figure 4.3). We then use this location and extension to fit HAWC's spectral energy distribution for the source. We include all energy bins which with a TS threshold of 1.5. We find that the power law index is best fit to -2.6 ± 0.2 and the flux normalization is 1.8 ± 0.4 E-14 cm^{-2} TeV^{-1} s^{-1} (see Equation 4.1). The preliminary spectrum for 2HWC J1949+244 is presented in Figure 4.4.

$$\left(\frac{dN}{dE}\right)_{1949} = 1.8\text{E-}14 \left(\frac{E}{7\ \text{TeV}}\right)^{-2.6} \text{cm}^{-2}\ \text{TeV}^{-1}\ \text{s}^{-1} \tag{4.1}$$

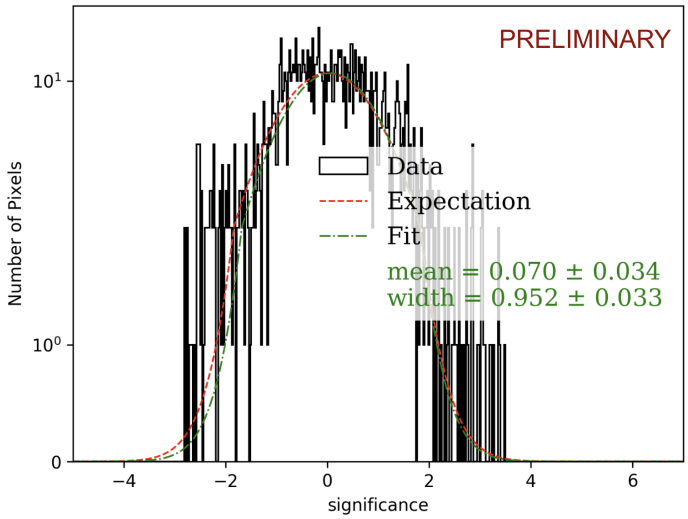

Figure 4.3: Preliminary 1D significance histogram of the residuals for 2HWC J1949+244.

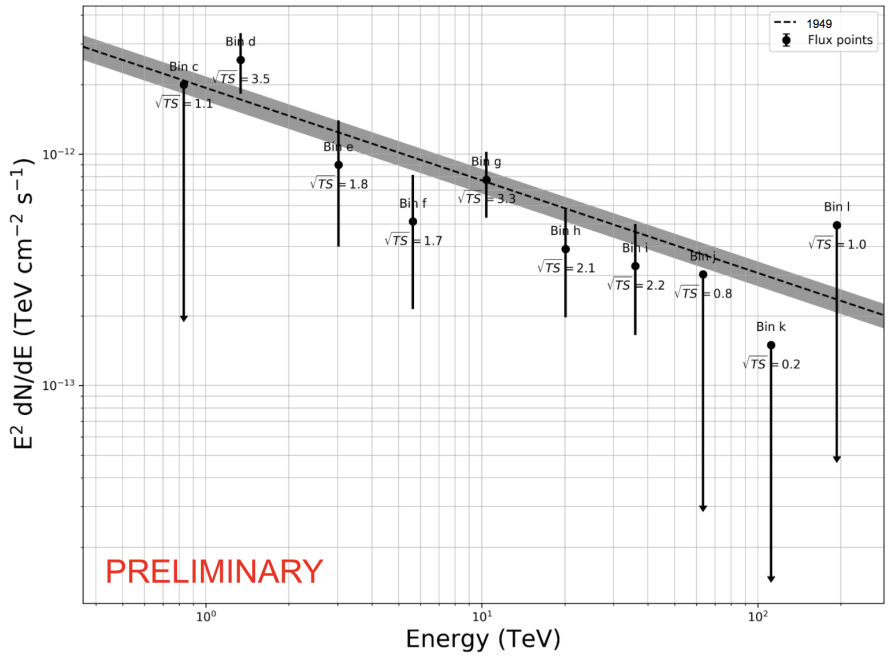

Figure 4.4: Preliminary Spectral Energy Distribution for 2HWC J1949+244. The power law fit has an index of -2.6 ± 0.2 and flux normalization of 1.8 ± 0.4 E-14 cm^{-2} TeV^{-1} s^{-1} (see Equation 4.1).

5.2.2 2HWC J1938+238

We then performed a similar analysis of the 2HWC J1938+238 region. We use a region of interest of 1°. We assume a simple power law spectrum with a pivot energy of 7 TeV and a Gaussian shape. We fit the extension of this region with the point of maximum significance in the 0.5° extended map, which is ($\alpha = 295.31^\circ$, $\delta = 23.93^\circ$). We find that the extension is best fit to $0.6 \pm 0.1^\circ$. We present maps of the region, source model, and residuals in Figure 4.5.

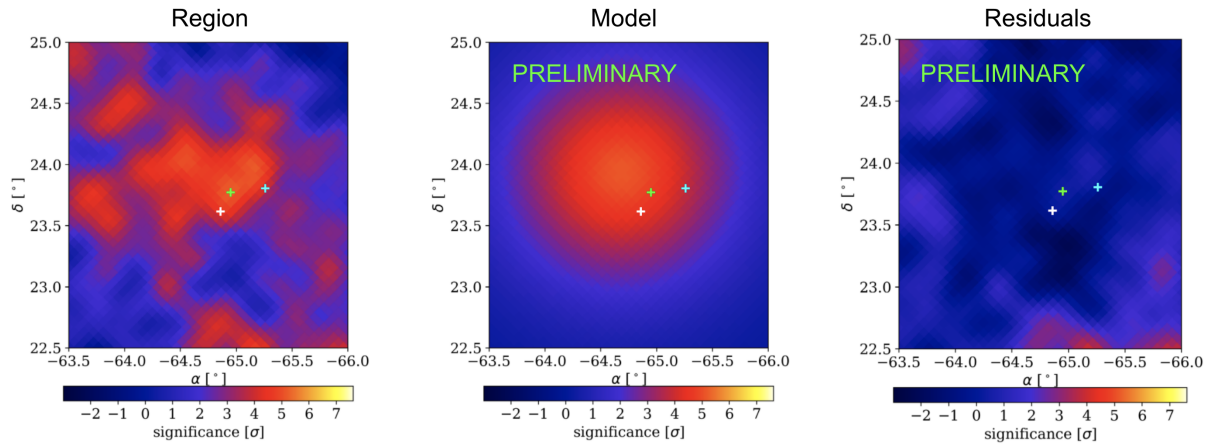

Figure 4.5: 3 maps of HAWC data for 2HWC J1938+238. The left map presents the region containing the source, the middle map presents the model for the source, and the right map presents the residuals. The white cross marks the location of PSR J1940+2337, the green cross marks the location of 3HWC J1940+237, and the cyan cross marks the location of 2HWC J1938+238 [49, 5, 4].

We expect the histogram of the residuals for this region to follow a Gaussian distribution with a mean of 0 and width of 1. We find that our data have a mean of 0.018 ± 0.033 and a width of 0.977 ± 0.032, which indicate that our model is a good fit (see Figure 4.6). We then use this location and extension to fit HAWC's spectral energy distribution for the source. We decide to include all energy bins which surpass a TS threshold of 1. We find that the power law index is best fit to -2.8 ± 0.2 and the flux normalization is 1.6 ± 0.4 E-14 cm^{-2} TeV^{-1} s^{-1} (see Equation 4.2). The preliminary spectrum for 2HWC J1949+244 is presented in Figure 4.4.

$$\left(\frac{dN}{dE}\right)_{1938} = 1.6\text{E-}14 \left(\frac{E}{7\text{ TeV}}\right)^{-2.8} \text{cm}^{-2}\text{ TeV}^{-1}\text{ s}^{-1} \tag{4.2}$$

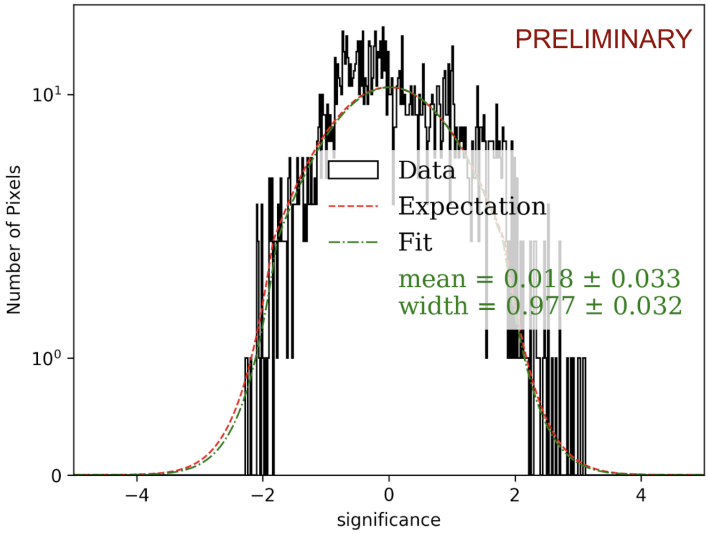

Figure 4.6: Preliminary 1D significance histogram of the residuals for 2HWC J1938+238.

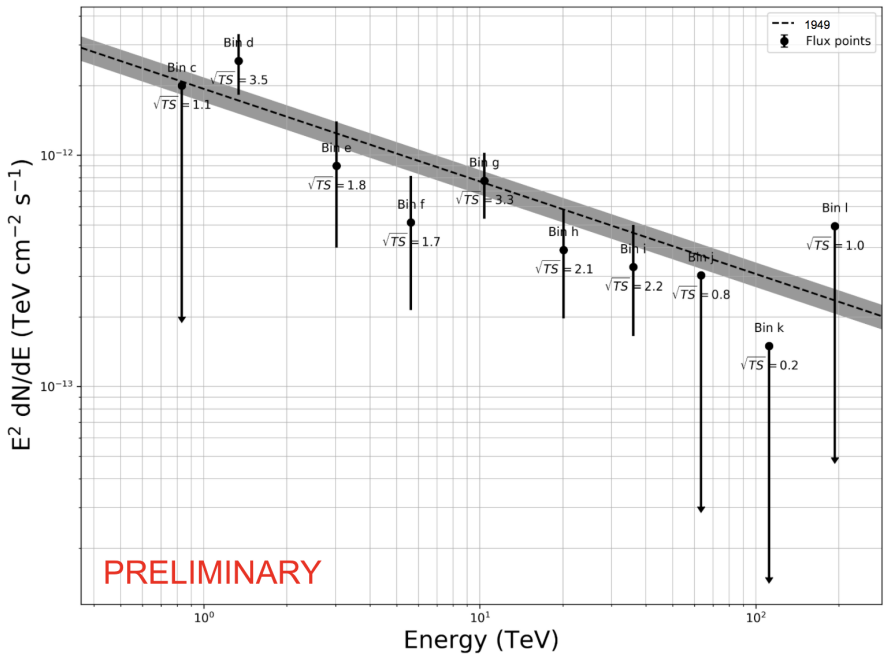

Figure 4.7: Preliminary Spectral Energy Distribution for 2HWC J1938+238. The power law fit has an index of -2.8 ± 0.2 and flux normalization of 1.6 ± 0.4 E-14 cm^{-2} TeV^{-1} s^{-1} (see Equation 4.1).

Bibliography

[1] P. Morrison. On gamma-ray astronomy. *Il Nuovo Cimento*, 7(6):858–865, 1958.

[2] Bernard Degrange and Gérard Fontaine. *Introduction to high-energy gamma-ray astronomy*. Elsevier, September 2015. https://www.sciencedirect.com/science/article/pii/S1631070515001292.

[3] HAWC Collaboration. HAWC. https://www.hawc-observatory.org/.

[4] A. U. Abeysekara, A. Albert, R. Alfaro, C. Alvarez, J. D. Álvarez, R. Arceo, J. C. Arteaga-Velázquez, H. A. Ayala Solares, A. S. Barber, B. Baughman, and et al. The 2HWC HAWC Observatory Gamma-Ray Catalog. *The Astrophysical Journal*, 843(1):40, June 2017. http://dx.doi.org/10.3847/1538-4357/aa7556.

[5] A. Albert and et al. 3HWC: The Third HAWC Catalog of Very-High-Energy Gamma-ray Sources. *arXiv.org*, January 2021. https://arxiv.org/abs/2007.08582.

[6] Stefan Funk. Ground- and Space-Based Gamma-Ray Astronomy. *Annual Review of Nuclear and Particle Science*, 65(1):245–277, October 2015. http://dx.doi.org/10.1146/annurev-nucl-102014-022036.

[7] Matteo Cerruti. Leptonic and Hadronic Radiative Processes in Supermassive-Black-Hole Jets. *arXiv.org*, December 2020. https://arxiv.org/abs/2012.13302.

[8] J. Gregory Stacy and W. Thomas Vestrand. *Gamma-Ray Astronomy*. Encyclopedia of Physical Science and Technology (Third Edition), 2003.

[9] Rui-Zhi Yang, Ervin Kafexhiu, and Felix Aharonian. Exploring the shape of the γ-ray spectrum around the "π^0-bump". *Astronomy & Astrophysics*, 2018. https://www.aanda.org/articles/aa/abs/2018/07/aa30908-17/aa30908-17.html.

[10] M. Ackermann, M. Ajello, A. Allafort, L. Baldini, J. Ballet, G. Barbiellini, M. G. Baring, D. Bastieri, K. Bechtol, R. Bellazzini, and et al. Detection of the Characteristic Pion-Decay Signature in Supernova Remnants. *arXiv.org*, (6121):807–811, February 2013. https://arxiv.org/abs/1302.3307.

[11] Elisa Prandini. Highlights from tev extragalactic sources. *arXiv.org*, July 2017. https://arxiv.org/abs/1706.01670.

[12] LAT Collaboration. Fermi Large Area Telescope Third Source Catalog. *arXiv.org*, June 2015. https://arxiv.org/abs/1501.02003.

[13] Lori Ann White. Fermi's First Five Years. *Symmetry Magazine*, August 2013. https://www.symmetrymagazine.org/article/august-2013/fermis-first-five-years.

[14] Rob Garner. Fermi Spacecraft and Instruments. *NASA*, October 2017. https://www.nasa.gov/content/goddard/fermi-spacecraft-and-instruments.

[15] Fermi LAT Collaboration. Fermi Data Online Documentation Science Tools. https://fermi.gsfc.nasa.gov/ssc/data/analysis/documentation/Cicerone/Cicerone_Introduction/LAT_overview.html.

[16] Nahee Park. VERITAS and Fermi-LAT observations of TeV gamma-ray sources from the second HAWC catalog. *arXiv*, 2017. https://arxiv.org/abs/1708.05744.

[17] Nicola Galante. VERITAS discovers very high energy gamma rays from the starburst galaxy m82. *National Science Foundation*. https://www.nsf.gov/news/news_images.jsp?cntn_id=115836&org=NSF.

[18] VERITAS. Whipple 10m Telescope and Blazar Lightcurves, September 2006. https://veritas.sao.arizona.edu/whipple.

[19] Stephanie Häffner. Studies of cosmic-ray electrons with the H.E.S.S. experiment using an advanced reconstruction technique. Master's thesis, U. Erlangen-Nuremberg (main), 2010.

[20] Ken Ragan. ACT Techniques & VERITAS Technology, January 2010. https://veritas.sao.arizona.edu/about-veritas/atmospheric-cherenkov-technique-and-veritas-technologies.

[21] A.U. Abeysekara, J.A. Aguilar, S. Aguilar, R. Alfaro, E. Almaraz, C. Álvarez, J. de D. Álvarez Romero, M. Álvarez, R. Arceo, J.C. Arteaga-Velázquez, and et al. On the sensitivity of the HAWC observatory to gamma-ray bursts. *Astroparticle Physics*, 35(10):641–650, May 2012. http://dx.doi.org/10.1016/j.astropartphys.2012.02.001.

[22] Andrew J. Smith. HAWC: Design, Operation, Reconstruction and Analysis. *arXiv.org*, August 2015. https://arxiv.org/abs/1508.05826.

[23] A Gonzalez Munoz. Latest news from the High Altitude Water Cherenkov Observatory, May 2016. https://www.researchgate.net/publication/305800309_Latest_news_from_the_High_Altitude__Cherenkov_Observatory/fulltext.

[24] Harm Schooriemmer. *Simulated Gamma-Ray Events*. Dec 2020.

[25] A. U. Abeysekara, A. Albert, R. Alfaro, C. Alvarez, J. D. Álvarez, R. Arceo, J. C. Arteaga-Velázquez, H. A. Ayala Solares, A. S. Barber, N. Bautista-Elivar, and et al. Observation of the Crab Nebula with the HAWC Gamma-Ray Observatory. *arXiv.org*, January 2017. https://arxiv.org/abs/1701.01778.

[26] A. A. Abdo, B. T. Allen, T. Aune, W. Benbow, D. Berley, C. Chen, G. E. Christopher, T. DeYoung, B. L. Dingus, R. W. Ellsworth, and et al. Observation and Spectral Measurements of the Crab Nebula with Milagro. *arXiv.org*, October 2011. https://arxiv.org/abs/1110.0409.

[27] Kathleen McGarvey. Catching some gamma rays in central Mexico. *NewsCenter*, October 2016. https://www.rochester.edu/newscenter/catching-some-gamma-rays-in-central-mexico-163572/.

[28] Holger Birk and Rolf T. Borlinghaus. Which Sensor is the Best for Confocal Imaging? *Learn & Share — Leica Microsystems*, July 2018. https://www.leica-microsystems.com/science-lab/which-sensor-is-the-best-for-confocal-imaging/.

[29] Henrike Fleischhack, Petra Huentemeyer, et al. Joint Likelihood Fits for the Study of Galactic Objects with HAWC. *arXiv preprint arXiv:1708.02955*, 2017.

[30] R Atkins, W Benbow, D Berley, E Blaufuss, J Bussons, DG Coyne, RS Delay, T DeYoung, BL Dingus, DE Dorfan, et al. Observation of tev gamma rays from the crab nebula with milagro using a new background rejection technique. *The Astrophysical Journal*, 595(2):803, 2003.

[31] S. S. Wilks. *The Large-Sample Distribution of the Likelihood Ratio for Testing Composite Hypotheses*. March 1938. https://projecteuclid.org/journals/annals-of-mathematical-statistics/volume-9/issue-1/The-Large-Sample-Distribution-of-the-Likelihood-Ratio-for-Testing/10.1214/aoms/1177732360.full.

[32] J. Patrick Harding. Introduction to Maximum Likelihood, November 2015. https://private.hawc-observatory.org/wiki/images/2/2f/Harding_llh-intro_2015-11-16.pdf.

[33] HAWC Collaboration. The Analysis and Event Reconstruction Integrated Environment (AERIE) (version 2.02.00). *GitLab repository*, 2015. https://gitlab.com/hawc-observatory/aerie.

[34] Giacomo Vianello, Robert J. Lauer, Patrick Younk, Luigi Tibaldo, James M. Burgess, Hugo Ayala, Patrick Harding, Michelle Hui, Nicola Omodei, Hao Zhou, and et al. The Multi-Mission Maximum Likelihood framework (3ML). *arXiv.org*, July 2015. https://arxiv.org/abs/1507.08343.

[35] Kelly Malone. HAWC Observatory Spectral fitting with energy estimators. August 2019. https://www.dropbox.com/s/mc7931t3ezebgw5/2398_04.pdf?dl=0.

[36] Chad Brisbois. HAWC Energy Binning Scheme. *GitLab repository*, 2019. https://gitlab.com/hawc-observatory/analysis-scripts/threeml-analysis-scripts/blob/master/fitModel/analysis_modules/hawc_bins.yml.

[37] A. U. Abeysekara and et al. VERITAS and Fermi-LAT Observations of TeV Gamma-Ray Sources Discovered by HAWC in the 2HWC Catalog. October 2018. https://iopscience.iop.org/article/10.3847/1538-4357/aade4e/pdf.

[38] Michael C. Stroh and Abe D. Falcone. Swift X-ray Telescope Monitoring of Fermi-LAT Gamma Ray Sources of Interest. *arXiv.org*, May 2013. https://arxiv.org/abs/1305.4949.

[39] HAWC Collaboration. Detailed analysis of the region surrounding the new TeV -ray source HAWC J1928+177* In Progress. 2020. https://private.hawc-observatory.org/wiki/index.php/Detailed_analysis_of_the_region_surrounding_the_new_TeV_gamma-ray_source_3HWC_J1928+178.

[40] Alberto Carraminana. The panoramic -ray view of Galactic cosmic accelerators at TeV energies with the HAWC observatory. *Nuclear and Particle Physics Proceedings*, October 2018. https://www.sciencedirect.com/science/article/pii/S2405601418301111.

[41] PSR J1940 2337. *PSR@DB Pulsar Database*, August 2020. http://www.psrdb.net/pulsar/85f33c8a85f3409e928675ca84a4a697/detail.

[42] W. W. Zhu and et al. Mass measurements for two binary pulsars discovered in the PALFA survey. *arXiv.org*, July 2019. https://arxiv.org/abs/1907.05046.

[43] XRT Survey of Fermi Unassociated Sources. https://www.swift.psu.edu/unassociated/.

[44] Miguel Araya. Exploring the nature of 2HWC J2006+341 with HAWC and Fermi-LAT. *arXiv.org*, July 2019. https://arxiv.org/abs/1907.10197.

[45] Javier Coronado-Blázquez and Miguel A. Sánchez-Conde. Constraints to Dark Matter Annihilation from High-Latitude HAWC Unidentified Sources. *Galaxies*, 8(1):5, December 2019. http://dx.doi.org/10.3390/galaxies8010005.

[46] E. Aliu, S. Archambault, T. Aune, B. Behera, M. Beilicke, W. Benbow, K. Berger, R. Bird, J. H. Buckley, V. Bugaev, and et al. INVESTIGATING THE TeV MORPHOLOGY OF MGRO J1908+06 WITH VERITAS. *The Astrophysical Journal*, 787(2):166, May 2014. http://dx.doi.org/10.1088/0004-637X/787/2/166.

[47] M. Salvato, J. Buchner, T. Budavári, T. Dwelly, A. Merloni, M. Brusa, A. Rau, S. Fotopoulou, and K. Nandra. Finding counterparts for all-sky X-ray surveys with Nway: a Bayesian algorithm for cross-matching multiple catalogues. *arXiv.org*, October 2017. https://arxiv.org/pdf/1705.10711.pdf.

[48] Cherenkov Telescope Array. https://www.cta-observatory.org/.

[49] Universite de Strasbourg. *SIMBAD Astronomical Database - CDS (Strasbourg)*. http://simbad.u-strasbg.fr/simbad/.

ACADEMIC VITAE - NICOLE M. FIRESTONE

EDUCATION

The Pennsylvania State University, Schreyer Honors College *Graduating May 2021*

- Bachelor's of Science in Physics, General Option
- Bachelor's of Science in Astronomy & Astrophysics, Graduate Studies Option
- Minor in Mathematics

RESEARCH

High Altitude Water Cherenkov Gamma-Ray Observatory (HAWC) *2019 - Present*
Research Assistant, Supervisor: Dr. Miguel Mostafá

- Detecting and analyzing gamma ray showers to determine locations of high energy astrophysical phenomena and performing correlation analysis with international data from AMON
- Analyzing new HAWC maps in cross reference with old HAWC survey data and other AMON observatory data to pinpoint unassociated candidate TeV sources, determine the likelihood of their existence, examine their morphology and energy spectra, and determine their classification

Laser Interferometer Gravitational-Wave Observatory (LIGO) *Summer 2020*
Research Assistant, Supervisor: Dr. Chad Hanna

- Worked on testing and running offline GstLAL-based inspiral pipeline for analysis of gravitational waves from the coalescence of compact binaries
- Created template banks, defined chunks, generated injection sets, and performed analysis of data for Advanced LIGO's third observing run (O3)

PROJECTS

Schreyer Honors Thesis in Physics and Astronomy & Astrophysics *2021*
Supervisor: Dr. Miguel Mostafá; Advisors: Dr. Richard Robinett and Dr. William Brandt

- Explaining the theory behind gamma ray astronomy, extensive air showers, particle decay, Cherenkov light, and the HAWC Observatory
- Compiling HAWC research to create a comprehensive TeV source analysis and updated unassociated source catalog

Nebulae, Galaxies, and Cosmology Honors Project *2020*

- Explored the relationship between the results of cosmological large-scale structure studies and the concept of "bias" by developing an understanding of the formation of structure in the early universe and examining the literature in the field

Nebulae, Galaxies, and Cosmology Mock Observing Proposal *2020*

- Developed a mock research project to probe the distribution of dark matter in galaxies via weak galaxy-galaxy gravitational lensing using the Subaru Telescope's Hyper Suprime-Cam

Observational Astronomy Final Project *2019*

- Performed observations with PlaneWave telescope to take images of star cluster in multiple filters
- Performed multi-aperture photometry in AstroImageJ to create an H-R diagram and determine the age of the cluster

Quantum Mechanics Honors Project *2019*

- Explained the mathematics and quantum mechanical theory behind nuclear magnetic resonance and explored its application in medicine through nuclear magnetic resonance imaging (MRI)

CONFERENCES & PRESENTATIONS

American Physical Society *Quarks 2 Cosmos* Conference; Virtual *April 2020*
Unassociated Candidate TeV Sources from HAWC, poster presentation

Penn State Astronomy Communication Project Fair; Virtual *April 2020*
HAWC Research in Gamma Ray Astronomy, oral presentation

HAWC Collaboration Meeting; Virtual *October 2020*
Unidentified Galactic Source Candidates from 2HWC/3HWC, oral presentation

APS Mid-Atlantic Section Meeting; Virtual *December 2020*
Unassociated Candidate TeV Sources from HAWC, oral presentation

APS Conference for Undergraduate Women in Physics; Virtual *January 2021*
Examining HAWC Source 3HWC J1950+242, oral presentation

Penn State Undergraduate Exhibition; Virtual *April 2021*
Analyzing Unassociated Candidate TeV Sources with HAWC, oral presentation

APS *Quarks 2 Cosmos* Conference; Virtual *April 2021*
Investigating Unassociated HAWC Sources in the Region l=52-62 Degrees,
intended oral presentation

ACCOMPLISHMENTS & AWARDS

Sigma Pi Sigma (ΣΠΣ) Physics Honors Society *2020 - Present*
Inducted by Penn State Physics Department

Dean's List *2017 - Present*
Recognized by Penn State University

Academic Excellence Scholarship *2017 - Present*
Awarded by Schreyer Honors College, Penn State University

Homer Braddock Science Scholarship *2017 - Present*
Awarded by Eberly College of Science, Penn State University

Bert Elsbach Honors Physics Scholarship *2019 - 2020*
Awarded by Physics Department and Schreyer Honors College, Penn State University

John and Elizabeth Holmes Teas Physics Scholarship *2020 - Present*
Awarded by Physics Department, Penn State University

University Science Engagement Grant *2019 - 2020*
Granted by Eberly College of Science, Penn State University

Nonprofit Research & Advocacy Grant *2018*
Granted by CARES Foundation

FUTURE of Physics Program at The California Institute of Technology *2020*
Nominated by Dr. Miguel Mostafá; Selected by Caltech, the Division of
Physics, Mathematics and Astronomy, and the Heising-Simons Foundation

The Student Representative for Braddock Scholarship Selection Committee *2021*
Selected by Dean Christopher Palma of Eberly College of Science, Penn State University

Top 20 for Jewish Rock Radio's Jewish Star Competition *2021*
Mentored by Jewish educator, musician, and consultant, Eliana Light

SKILLS

Coding
Java, Python, LaTeX, Mathematica, Unix, Bash, R

Technical
X-ray fluorescence spectroscopy, cosmic ray telescope operation, telescope operation, laser operation, multi-aperture color photometry, deep sky astrophotography

Astronomy/Physics Software
AstroImageJ, SAOImageDS9, MaxIm DL, Nebulosity, DppMCA, CurcuitMaker

Office Software
Microsoft Word, Microsoft PowerPoint, Microsoft Excel, Google Docs, Google Slides, Google Sheets

Artistic Software
Canva, Wix, MuseScore, GarageBand, iMovie, Wondershare Filmora9, Adobe Premiere Pro

WORK EXPERIENCE

Ordinary and Partial Differential Equations Grader *2019*
Penn State Department of Mathematics

- Worked with Professor Zachary Tseng
- Graded homework, graded exams, and kept record of grades for three sections of the course

Exam Proctor *2019*
Penn State Department of Mathematics

Co-Director of Ritual and Spiritual Life *2019 - Present*
Penn State Cultural Organization

- Organize and plan weekly events, educational programs, discussions, and meetings; Apply for micro-grants to host events; Manage and designate tasks of committee members; Established consistency in events, and fostered a warm and welcoming environment for students of all backgrounds; Increased event attendance by six-fold

Ruach Intern, Sabbath Service Leader *2018 - Present*
Penn State Cultural Organization

Video and Audio Producer *2020 - Present*
Space Dragon Productions

ADVOCACY WORK

I Am Late Onset CAH Campaign *2018 - Present*
Founder and Head Research Advocate

- Created Campaign to inform pediatricians, gynecologists, and females ages six and older of what Late Onset Congenital Adrenal Hyperplasia (CAH) is so that females with Late Onset CAH do not have to face the struggles of misdiagnoses, the distress and confusion of not knowing what is wrong, or the long-term complications of having CAH; Reached an audience across nine countries; Recognized as an Endocrine and Puberty Center resource by the Children's Hospital of Philadelphia

Adrenal Alternatives Foundation *2019*
Congenital Adrenal Hyperplasia Advocate

ACTIVITIES

Penn State Honors Physics Outreach Program *2017 - Present*
Information Session Leader, Student Engager

Penn State Society of Physics Students *2017 - Present*
Member

None Of The Above (NOTA) A Cappella *2018 - Present*
Music Director (2020-Present), Assistant Music Director (2019-20), Arranger, Soloist

Penn State University Choir *2017 - 2020*
Soprano 1 Section Leader

Penn State Oriana Singers Premier Women's Choir *2019 - 2020*
Member

Penn State Hebrew Club *2020 - Present*
Vice President

Penn State Concert Band *2017*
First Clarinet

COMMUNITY SERVICE

Trenton Area Soup Kitchen *2017 - Present*
Volunteer

Greenwood House Senior Living Care *2015 - Present*
Musical Entertainer, Service Leader

Schreyer Honors College Student Council *2017*
Service Committee Member

Please visit me at https://music4ev4.wixsite.com/nicolemfirestone.